

# Germanium Photodetector Technologies for Optical Communication Applications

Kah-Wee Ang, Guo-Qiang Lo and Dim-Lee Kwong  
*Institute of Microelectronics, Agency for Science, Technology & Research (A\*STAR)*  
Singapore

## 1. Introduction

Converging computing and communication capabilities on single chip platform is becoming increasingly important to keep up with the performance roadmap known as Moore's Law (Kimerling et al., 2006). Today, data transmissions at a bit-rate of 10 Gb/s over long distance makes photonic interconnection an easier approach to implement than electrical interconnect. At this data rate, the conventional copper solution has begun to encounter extreme challenges related to power consumption and reach (Wada et al., 2002). Moreover, the growing issues in electro-magnetic interference, signal cross-talk, and heavier weight make it an inferior approach for high bandwidth applications (Gunn, 2006). To keep up with the scaling of interconnect bandwidth, an alternative solution makes use of optical interconnect technology to meet the ever increasing bit rate requirement of data communication. Over the past decades, conventional optical components were typically made of exotic III-V compound materials such as gallium-arsenide (GaAs) and indium-phosphide (InP) due to their excellent light emission and absorption properties. Unfortunately, compound-semiconductor devices are generally too complicated to process and costly to implement in optical interconnects.

In search for a cost-effective solution, Si photonic emerges to hold great promise for its inexpensive material and its compatibility with current complementary metal-oxide-semiconductor (CMOS) process technology (Soref, 2006). However to make silicon photonic communication a reality, several key technological challenges have to be addressed. Inferior optical properties of Si have thus far the major show-stopper to preclude the development of a key active photonic component needed to perform optical to electrical encoding. Very recently, germanium (Ge) has attracted growing interest for the realization of high performance photodetector due to its favourable absorption coefficient (Hartmann et al., 2004). However, Ge can be a challenging material to integrate in a CMOS environment for its low thermal budget constraint and its large lattice mismatch of ~4.2% with Si (Luan et al., 1999). High defect densities seen in the Ge-on-Silicon-on-Insulator (Ge-on-SOI) epitaxial film could induce unfavourable carrier recombination process that would degrade the detector's quantum efficiency.

In this chapter, the current development of optical detection technologies on silicon photonics platform is reviewed. The discussion first begins with the development of Ge-on-

SOI hetero-epitaxy process technology. The approach, based on the low temperature pseudo-graded silicon-germanium buffer engineering, is adopted to relieve the large lattice mismatch of ~4.2% between the two heterostructure materials. This enables a high quality Ge epitaxy film with low threading dislocation density to be grown on Si. The subsequent sections of this chapter deal with the state-of-the-art Ge photodetector technologies. We begin with the discussion on the designs of evanescent-coupled Ge *p-i-n* photodetector featuring an integrated SOI micro-waveguide. Performance metrics in these detectors in terms of dark current, responsivity, and bandwidth are evaluated. The mechanism accountable for the leakage generation in such device and its dependence on the applied electric field strength are elucidated. Factors limiting the detector speed performance and guidelines to enable bandwidth scaling are also discussed.

This chapter also aims to discuss the demonstration of Schottky barrier engineered Ge photodetector featuring metal-semiconductor-metal (MSM) configuration. The problem and mechanism responsible for the generation of high leakage current in such a detector are dealt with. Novel concepts adopted to address this issue through Schottky barrier modulation are presented. The approaches are based on bandgap engineering as well as Fermi level de-pinning by segregating valence mending adsorbate near the metal/germanium interface. The recent technological breakthrough in employing all Group-IV based materials to realize high gain-bandwidth product Ge/Si avalanche photodetector (APD) is presented next. The fabrication process and the design of Ge/Si APD featuring separate-absorption-charge-multiplication (SACM) configuration are discussed. We conclude the chapter with a summary providing the readers with the comparative views on the performance metrics of the various Ge-based photodetector schemes.

## 2. Hetero-Epitaxy of Germanium on Silicon

The key challenge to high quality germanium (Ge) epitaxy growth on silicon (Si) rests with the huge lattice mismatch between the two heterostructure materials. The existence of ~4.2% lattice mismatch strain has been shown to give rise to two major issues: (1) high densities of threading dislocations and (2) rough surface morphology due to 3D Stranski-Krastanov (SK) growth. Both of these defects present much concerns for the generation of high leakage current which would compromise the efficiency of a photodetector. Strategies proposed in the literature to overcome these challenges vary to a large extent. One most intuitive approach is to grow a silicon-germanium (SiGe) layer by compositionally grading its Ge concentration up to 100%. Using low-energy plasma enhanced chemical vapour deposition, Oh et al. (2002) showed that for every 10% increase in the Ge mole fraction, a linearly graded SiGe buffer of ~1 $\mu\text{m}$  thickness is required. This results in a need to grow a relatively thick SiGe buffer layer of 10 $\mu\text{m}$  before a low dislocation density Ge epilayer can be deposited, which imposes much difficulties for process integration.

In an effort to further reduce the thickness of these active layers, Huang et al. (2004) proposed another approach based on the optimization of two thin SiGe buffer layers with varying Ge concentration. In such approach, a 0.6 $\mu\text{m}$  thick Si<sub>0.45</sub>Ge<sub>0.55</sub> buffer was first grown and then followed by an intermediate Si<sub>0.35</sub>Ge<sub>0.65</sub> buffer with a thickness of 0.4 $\mu\text{m}$ . An in-situ annealing for 15 min at 750°C was subsequently performed to further reduce the dislocation density before the growth of a 2.5 $\mu\text{m}$  thick Ge epilayer at a process temperature of 400°C. Through this approach, it allows the threading dislocations to be trapped at the hetero-

interfaces. This enables a significant reduction in the dislocation density of the as-grown Ge epilayer, thereby improving the detector's dark current performance.

In yet another approach, Colace et al. (1999) proposed a direct hetero-epitaxy growth of Ge on Si through the use of a low temperature thin SiGe buffer layer (a few 10nm). The insertion of such thin buffer avoids the occurrence of 3D SK growth, and allows the misfit dislocations to be concentrated at the hetero-interfaces. However such approach requires a cyclic annealing process to be carried out at both high and low temperature (900°C/780°C) to reduce the threading dislocation density within the Ge active film. Using a similar cyclic thermal annealing approach, Luan et al. (1999) had also demonstrated a significant improvement in both the surface roughness and the dislocation density. When combined with the selective area growth, an average threading dislocation density as low as  $2.3 \times 10^6 \text{ cm}^{-2}$  was achieved. However, the needs for a high temperature post-epitaxy Ge anneal with long cycle time present a major concern for CMOS implementation.

In this work, selective epitaxial growth of Ge on silicon-on-insulator (SOI) was performed using an ultra-high vacuum chemical vapor deposition (Ang et al., 2010) reactor. Unlike the conventional approaches, a thin pseudo-graded SiGe buffer with a thickness of  $\sim 20\text{nm}$  is proposed in this study to relieve the large lattice mismatch stress between the two heterostructure materials (Fig. 1). The Ge mole fraction within the SiGe buffer is compositionally graded from 10% to  $\sim 50\%$ . The precursor gases used for the SiGe growth comprise of diluted germane ( $\text{GeH}_4$ ) and pure disilane ( $\text{Si}_2\text{H}_6$ ). A relatively thin Ge seed layer of  $\sim 30\text{nm}$  is subsequently grown on the SiGe buffer at a process temperature of  $370^\circ\text{C}$ . The use of a low temperature growth is intended to suppress adatoms migration on Si and thus prevents the formation of 3D SK growth, which allows a flat Ge surface morphology to be achieved. Upon obtaining a smooth Ge seed layer, the epitaxy process temperature is then increased to  $\sim 550^\circ\text{C}$  to facilitate faster epitaxy growth to obtain the desired Ge thickness. Using this approach, high quality Ge epilayer with a thickness of up to  $\sim 2\mu\text{m}$  has been demonstrated, along with the achievement of threading dislocation density as low as  $\sim 10^7 \text{ cm}^{-2}$  without undergoing any high temperature cyclical thermal annealing step.

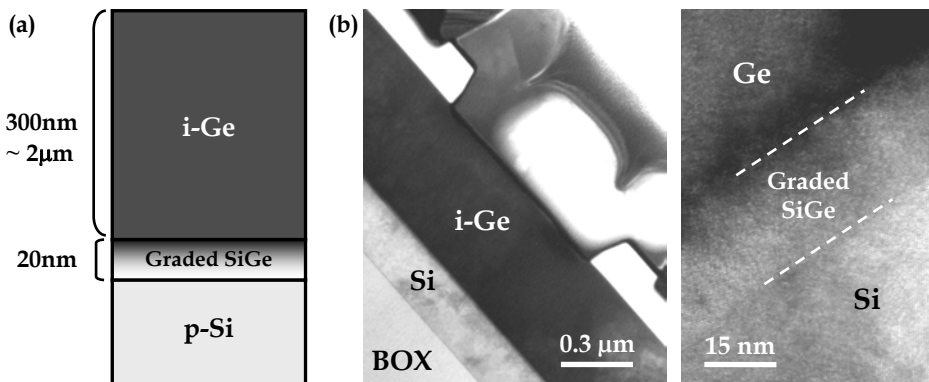


Fig. 1. (a) Schematic view of the layer stack for the direct hetero-epitaxy growth of Ge on Si. (b) High resolution TEM micrograph showing the effectiveness of a pseudo-graded SiGe buffer in reducing the threading dislocation density within the Ge epilayer.

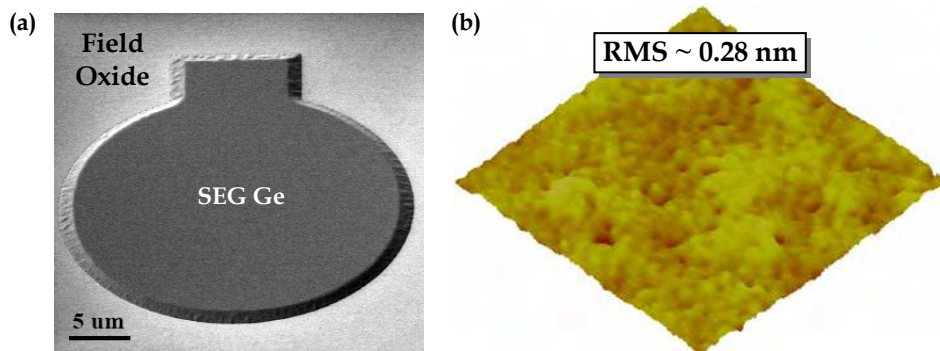


Fig. 2. (a) Scanning electron microscopy (SEM) image showing the achievement of excellent Ge epitaxy growth and selectivity on SOI substrate. (b) Excellent Ge surface roughness of  $\sim 0.28\text{nm}$  was achieved, as determined using atomic force microscopy (AFM).

In addition, selective area growth of Ge on Si has also been developed using a cyclical deposition and etch back approach. In each deposition cycle, the Ge growth time is carefully optimized to avoid exceeding the incubation time needed for Ge seeds to nucleate on the dielectric film. After every Ge deposition cycle, a short etch back process using chlorine ( $\text{Cl}_2$ ) precursor gas will then be introduced to remove possible Ge nucleation sites on the dielectric. This allows a highly selective Ge epitaxy process to be developed, along with the achievement of excellent surface roughness of  $\sim 0.28\text{nm}$  (Fig. 2).

### 3. High Performance Germanium *p-i-n* Photodetector

Due to its poor absorption coefficient as inherited by the large bandgap energy, silicon (Si) has been known to be prohibitive for the realization of photodetector that is capable of performing efficient optical detections at wavelengths commonly used in optical fiber communication ( $1.31\sim 1.55\mu\text{m}$ ). This can be addressed by introducing a new material with a smaller bandgap energy such as germanium (Ge) to provide favorable optical absorption property at these wavelengths. Recent research progress made in the photodetector technology development has clearly shown that Ge is attracting growing interest as the preferred photo-absorbing material due to its much higher absorption coefficient as compared to that of Si (Hartmann et al., 2002). In addition, its compatibility with current CMOS fabrication technology makes it an attractive material to enable the demonstration of high performance near-infrared photodetector (Soref, 2006).

However, the long absorption length in Ge at  $1.55\mu\text{m}$  wavelength renders it difficult to meet the high quantum efficiency requirement for a surface illuminated photodetector. Despite the use of a  $\sim 1\mu\text{m}$  Ge active layer, Colace et al. (2007) reported the achievement of a maximum responsivity of merely  $0.2\text{A/W}$  at  $1.55\mu\text{m}$  wavelength. One way to overcome this constraint requires the growth of a thick Ge epilayer to enable full absorption at this wavelength. Unfortunately, hetero-epitaxy of Ge with such thickness imposes much process integration challenge such as high threading dislocation densities that would lead to increased leakage current and thus degrade the receiver sensitivity. An alternative approach to relax this requirement makes use of a waveguide based photodetector (Yin et al., 2007).

By leveraging on the detector length, one would be able to achieve enhanced photo-detection efficiency and thus responsivity improvement. In addition, the bandwidth performance of the photodetector can also be simultaneously optimized by tweaking the Ge thickness to reduce the carrier transit time delay.

In this section, the different designs of waveguide integrated Ge photodetector featuring *p-i-n* configuration are discussed. The performance metrics such as dark current, responsivity, and bandwidth in these devices are evaluated and compared.

### 3.1 Ge-on-SOI Photodetector Designs and Fabrication

Two types of evanescent butt-coupled Ge-on-SOI photodetector design are shown in Fig. 3. Photodetectors featuring vertical *p-i-n* (VPD) and lateral *p-i-n* (LPD) configurations were fabricated, with Ge active layer selectively grown and integrated on a SOI micro-waveguide. For the VPD, the p+ and n+ junctions were formed in the Si and Ge regions, respectively, with the intrinsic region thickness ( $t_{i-Ge}$ ) co-defined by the Ge thickness ( $t_{Ge}$ ) and the thickness of the n+ implant region [Fig. 3(a)]. The width  $W$  and length  $L$  of this VPD design is  $8\mu\text{m}$  and  $100\mu\text{m}$ , respectively. For the LPD design, both the p+ and n+ junctions were formed in the Ge region, with the width of the intrinsic region ( $w_{i-Ge}$ ) determined by defining the spacing of these alternating contacts [Fig. 3(b)]. Note that the width  $W$  and length  $L$  of this LPD design is  $20\mu\text{m}$  and  $100\mu\text{m}$ , respectively.

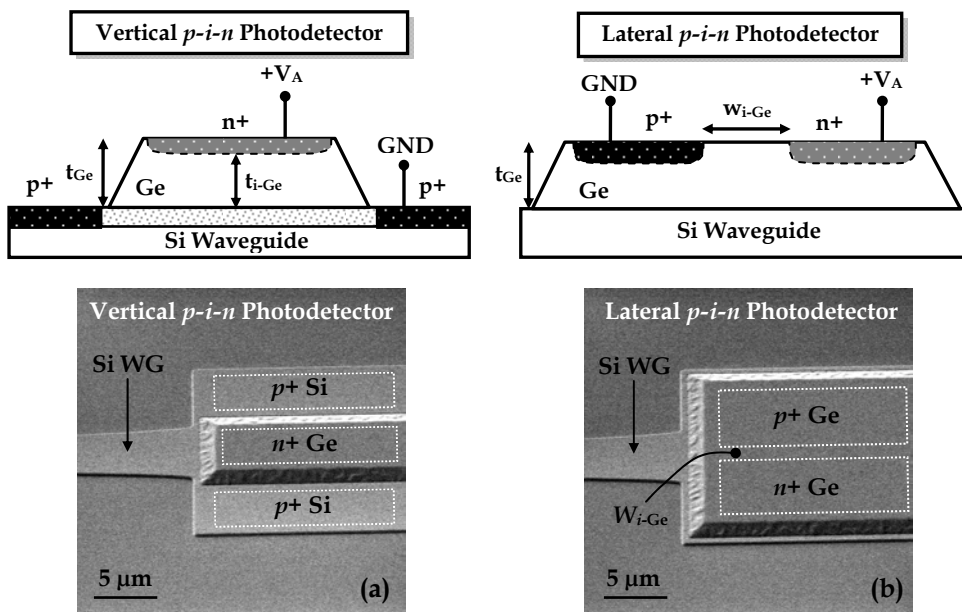


Fig. 3. (a) SEM micrograph showing the design of an evanescent butt-coupled Ge photodetector featuring vertical *p-i-n* configuration. (b) Ge photodetector design with a lateral *p-i-n* configuration.

By employing a waveguide-coupled design, the requirement for thick Ge epilayer to enhance the responsivity performance can be greatly relieved as one can leverage on the detector length to improve the optical absorption efficiency. As a result of the difference in the refractive index between Si and Ge, the incident photon traveling in the SOI micro-waveguide will be up-coupled into the Ge absorbing layer to allow optical signal to be encoded into its electrical equivalent efficiently. The insertion of a thick buried oxide (BOX) of  $\sim 2\mu\text{m}$  serves to confine the optical mode within the core of the channel waveguide so as to prevent leakage into the underneath Si substrate.

The fabrication process of the waveguide integrated Ge photodetector begins with the use of SOI substrate with a starting overlying Si thickness of  $\sim 220\text{nm}$  and a buried oxide (BOX) thickness of  $\sim 2\mu\text{m}$ . Channel waveguide with a nano-taper featuring a width of  $\sim 200\text{nm}$  was first formed by anisotropic dry etching to obtain a smooth sidewall profile for enabling low waveguide propagation loss. Ion implantation employing boron species was selectively done to form the Si anodes in a VPD detector. A moderately high p-type doping concentration was carefully chosen for the anode formation to ensure low series resistance while not impact the quality of the as-grown Ge epitaxy film. High dose p+ contact implant was subsequently performed and dopants are activated using rapid thermal anneal at  $1030^\circ\text{C}$  for 5s to obtain good Si ohmic contacts. After depositing a  $600\text{\AA}$  thick field oxide as passivation layer, a combination of anisotropic dry etch and followed by wet etch approach was adopted to preserve the top Si surface quality from possible damage by the reactive ion etching process. Hetero-epitaxy of Ge was then selectively grown in an ultra-high vacuum chemical vapor deposition (UHVCVD) epitaxy reactor. The selective Ge epitaxy process commenced with the deposition of a low temperature pseudo-graded silicon-germanium buffer ( $\sim 20\text{nm}$ ) and followed by a Ge seed layer with a thickness of  $\sim 30\text{nm}$ . A cyclical deposition and etch back approach was then used to raise the Ge thickness to  $\sim 500\text{nm}$ . Due to the achievement of low defects level within the Ge film, the high temperature post-epitaxy Ge anneal typically used for defects annihilation was skipped to reduce the overall thermal budget. High dose selective phosphorous and boron implants were then performed in a LPD and annealed at  $500^\circ\text{C}$  for 5 min to form good n-type and p-type Ge ohmic contacts, respectively. After the deposition of inter-layer dielectric (ILD), contact and metallization were subsequently done to complete the device fabrication. Fig. 3(a) and 3(b) show the top-view scanning electron microscopy (SEM) images of the VPD and LPD detectors, respectively.

### 3.2 Dark Current Characteristics

Dark current plays a vital role in affecting the shot noise ( $I_S$ ) in a photodetector according to the following expression

$$I_S^2 = 2 q B (I_D + I_B) \quad (1)$$

where  $q$  denotes the elemental charge,  $B$  the bandwidth,  $I_D$  the dark current of the detector, and  $I_B$  the photocurrent due to background radiation. Under a carefully controlled situation,  $I_B$  is usually small and can therefore be neglected. However, thermal generation and/or defects-assisted tunnelling current due to strong electric field give rise to considerable dark current which degrades the shot noise and thus affects the signal-to-noise (SNR) ratio.

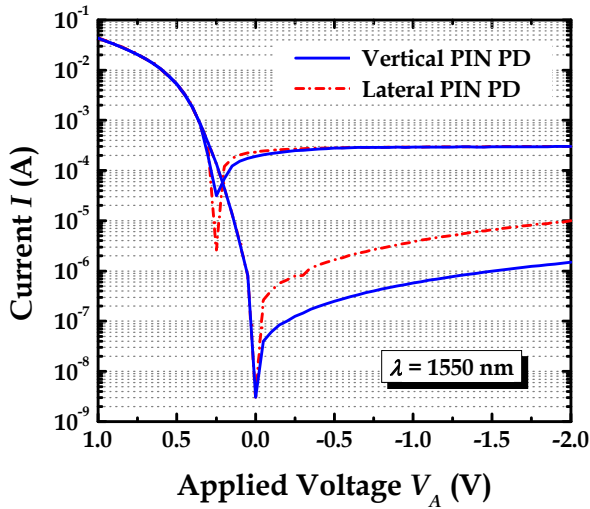


Fig. 4. The current-voltage characteristics of the VPD and LPD detectors measured under dark and illumination conditions.

Fig. 4 examines the current-voltage characteristics of the VPD and LPD detectors under dark and illumination conditions. Excellent rectifying characteristics were demonstrated in both the detectors, showing a forward-to-reverse current ratio of ~4 orders of magnitude. For a given applied bias of -1.0V, the dark current ( $I_{dark}$ ) in a VPD was measured to be ~0.57μA (or ~0.7nA/μm<sup>2</sup>), which is below the typical 1.0μA generally considered to be the upper limit for high speed receiver design. On the other hand, the dark current performance in a LPD showed a much higher  $I_{dark}$  value of ~3.8μA (or ~1.9nA/μm<sup>2</sup>). In order to better understand the factors which affect the dark current density ( $J_{Dark}$ ), let us review the expression that governs the leakage generation in a semiconductor diode

$$J_{Dark} = \frac{qn_i d}{\tau_{eff}} \tag{2}$$

where  $q$  denotes the elemental charge,  $n_i$  the intrinsic carrier density,  $d$  the depletion layer width, and  $\tau_{eff}$  the effective carrier lifetime. Clearly, an increase in the depletion layer width leads to a detrimental impact on the dark current performance, which could possibly explain the higher  $I_{dark}$  experienced in a LPD detector. In addition, it is also important to note that  $I_{dark}$  exhibits a strong dependence on the effective carrier lifetime which is controlled by both the lifetime associated with the Shockley-Read-Hall recombination ( $\tau_{SRH}$ ) and the carrier drift time across the space charge region ( $\tau_{drift}$ ) as follow

$$\frac{1}{\tau_{eff}} = \frac{1}{\tau_{SRH}} + \frac{1}{\tau_{drift}} \tag{3}$$

$$\tau_{SRH} = \frac{1}{\sigma v_{th} N_{TD} N_D} \quad (4)$$

$$\tau_{drift} = \frac{d}{\mu E} \quad (5)$$

where  $\sigma$  denotes the capture cross section,  $v_{th}$  the carriers thermal velocity,  $N_{TD}$  the threading dislocation density,  $N_D$  the density of recombination centres,  $\mu$  the low-field carrier mobility and  $E$  the electric field strength. It is obvious that the reverse dark current density should be proportional to the defects density within the Ge epilayer and a careful control of the epitaxy quality would be important to reduce the leakage current. Furthermore, an increase in the applied reverse bias has also resulted in an aggravated dark current degradation, which elucidates that  $I_{dark}$  has a strong dependence on the electric field strength. A further analysis on this phenomenon will be covered in a later discussion (see section 3.5).

### 3.3 Responsivity Characteristics

The responsivity ( $\mathfrak{R}$ ) of a photodetector can be described using the following expression

$$\mathfrak{R} = I_{Photo} / P_{Opt} = \eta q / h\nu \quad (6)$$

where  $I_{Photo}$  denotes the photocurrent,  $P_{Opt}$  the incident optical power,  $\eta$  the quantum efficiency,  $q$  the elemental charge,  $h$  the Planck constant, and  $\nu$  the frequency. In general, the incident photons which are absorbed in germanium generate electron-hole pairs which will be collected as photocurrent under applied electric field. This photocurrent is linearly dependent on the incident optical power before saturation is reached. Moreover, alike the quantum efficiency, the responsivity of the detector should be wavelength dependent. Hence, the responsivity of a detector will be significantly higher at wavelength where the photon energy enables electron-hole pair generation through direct transition.

In order to compare the responsivity performance between the VPD and LPD, optical measurements were performed by injecting an incident photon with a wavelength of 1550nm into the SOI micro-waveguide. The typical optical propagation loss in our SOI micro-waveguide under TE polarization mode is  $\sim 2$ dB/cm. No coupler was integrated with the Si waveguide and the incidence light was coupled through a single mode lensed fiber directly into the Si nano-taper. For an incident light power of  $\sim 300\mu W$ , optical measurements showed that both the VPD and LPD detectors achieved a comparable photocurrent level at high applied biases beyond -1.0V. Fig. 5 compares the responsivity of the detectors as a function of the applied voltages. It is interesting to note that the vertical PIN detector demonstrated a lower responsivity as compared to the lateral PIN detector for biases below -0.5 V. This could possibly be due to an enhanced carrier recombination process at the high density of defect centres near the Ge-Si heterojunction. This is set to compromise the absolute photocurrent value of a vertical PIN detector under low field influence. However with an increased electrostatic potential across the depletion layer, the photo-generated carriers can be assisted across the space charge region with enhanced mobility before they can recombine at these recombination centres.

For an applied bias larger than  $-1.0$  V, a comparable responsivity was measured for both the vertical and lateral PIN detectors. Despite that the metallurgical junction is separated by merely  $0.8\mu\text{m}$ , a lateral PIN detector showed a high absolute responsivity of  $\sim 0.9$  A/W. The possible mechanisms accountable for such high responsivity could be attributed to the following reasons. Firstly, under high reversed bias, the intrinsic Ge region (i.e. between and beneath the metallurgical junction) was simulated to be totally depleted, as confirmed using MEDICI device simulator. When photon is absorbed to produce electron and hole pairs, the fringe field beneath the metallurgical junction enables the generated carriers to be collected by the electrode as photocurrent. Secondly, optical simulation shows that more than 80% of the incidence light travelling in the SOI waveguide is absorbed within the first  $25\mu\text{m}$  of the detector. Hence by leveraging on the long absorption length design, nearly all incidence photons will be expected to contribute to the achievement of high responsivity.

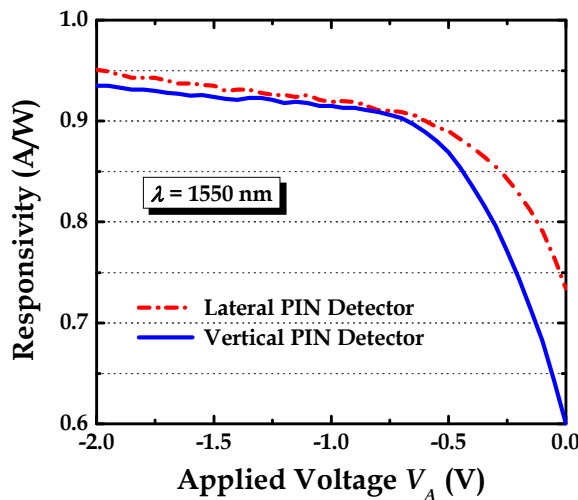


Fig. 5. Responsivity as a function of applied voltages for both the VPD and LPD detectors measured at a wavelength of 1550nm.

**3.4 Impulse Response Characteristics**

The impulse response of a photodetector is limited by both the carrier transit time ( $f_{Transit}$ ) and the RC time constant ( $f_{RC}$ ) which can be modelled using the following expressions

$$f_{Transit} = \frac{0.45 v_{sat}}{t_{i-Ge}} \tag{7}$$

$$f_{RC} = \frac{1}{2\pi RC} \tag{8}$$

where  $v_{Sat}$  denotes the carrier saturation velocity,  $d$  the depletion layer width, and  $RC$  the resistances and capacitances associated with the detector and its peripheral circuitry.

As described in these equations, the factors governing the fundamental response time limit of a detector lie with (1) the carrier drift time across the space charge region, and (2) the device junction capacitance. Drift of carriers is influenced by the electric field applied across the space charge region and can be expressed using

$$v_{\text{drift}} = \mu \cdot E \quad (9)$$

where  $\mu$  denotes the carrier mobility, and  $E$  the electric field. Clearly, increasing the electric field would enhance the drift velocity across the space charge region until a saturation velocity is reached. Sze (1981) showed that the carrier saturation velocity in germanium is on the order of  $\sim 10^7$  cm/s. In addition, the higher carrier mobility in Ge as compared to that of Si makes it a material of choice to enable the realization of high speed photodetector. On the other hand, decreasing the junction capacitance would allow one to achieve a reduced RC time constant. The junction capacitance ( $C_j$ ) which arises from the ionized donors ( $N_D$ ) and acceptors ( $N_A$ ) is expressed as follow

$$C_j = \epsilon A \left[ \frac{q}{2\epsilon(V_o - V)} \frac{N_D N_A}{N_D + N_A} \right]^{1/2} = \frac{\epsilon \cdot A}{W} \quad (10)$$

where  $\epsilon$  denotes the material permittivity,  $A$  the cross-sectional area of the detector, and  $W$  the depletion layer width. Intuitively, reducing the device area and increasing the depletion layer width are both beneficial to reduce the junction capacitance. However, adopting the former approach could lead to a compromise in the responsivity performance as the effective area for optical absorption is decreased. The latter approach in enlarging the depletion width could serve to enhance the response time as a result of lower junction capacitance. However, further increase in the depletion width would eventually lead to a degraded transit time across the space charge region. Therefore, an optimization of the RC time constant and the carrier transit time will be crucial in determining the overall bandwidth performance of the detector, as dictated using the following expression

$$f_{3\text{dB}} = \sqrt{\frac{1}{1/f_{\text{Transit}}^2 + 1/f_{\text{RC}}^2}} \quad (11)$$

In order to investigate the factors affecting the speed performance of the VPD and LPD detectors used in this study, impulse response measurements were performed at a photon wavelength of 1550nm. A pulsed laser source having a 80fs pulse width was used in the measurements. Both the detectors were characterized using microwave probes and the impulse responses were captured with a high speed sampling oscilloscope. Fig. 6 shows that a VPD detector achieved a smaller full-width-at-half-maximum (FWHM) pulse width of  $\sim 24.4$ ps as compared to that of LPD detector with a slightly larger FWHM of  $\sim 28.9$ ps. This could be attributed to the smaller depletion layer width design in a VPD detector which reduces the carrier transit time. The FWHM pulse width is related to the bandwidth and can be used as a metric to gauge the speed performance of the detectors. By performing a fast Fourier transform of the impulse responses, a  $-3\text{dB}$  bandwidth of  $\sim 11.3$  and  $\sim 10.1$  GHz were achieved in the VPD and LPD detectors, respectively.

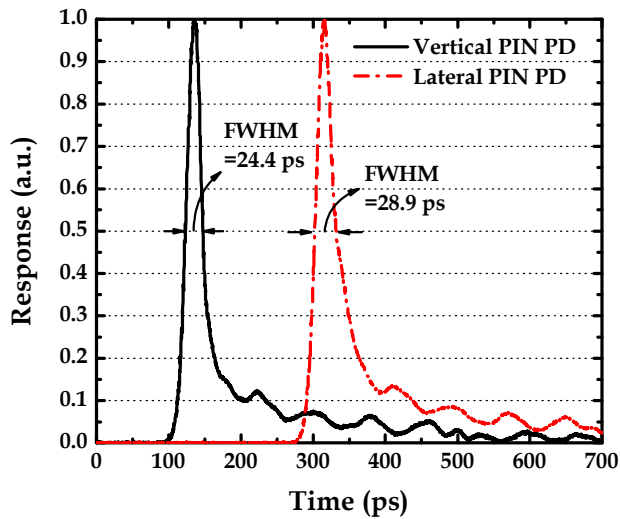


Fig. 6. Impulse responses of the VPD and LPD detectors measured at a wavelength of 1550nm. A smaller FWHM pulse width of  $\sim 24.4$  ps was achieved in a VPD as compared to a LPD, which corresponds to a  $-3$ dB bandwidth of  $\sim 11.3$  GHz.

The detector's bandwidth can be further evidenced by the eye patterns measurements (PRBS  $2^7-1$ ) done by directly connecting the output of the detector to the  $50\ \Omega$  electrical input of the DCA. Fig. 7 shows that high sensitivity and low-noise photo-detection up to a bit-rate of 8.5Gb/s can be achieved by the VPD detector. The clean eye patterns clearly illustrate the low noise property of the detector. Higher speed measurements are possible through further scaling of the detector geometry to reduce the device capacitance.

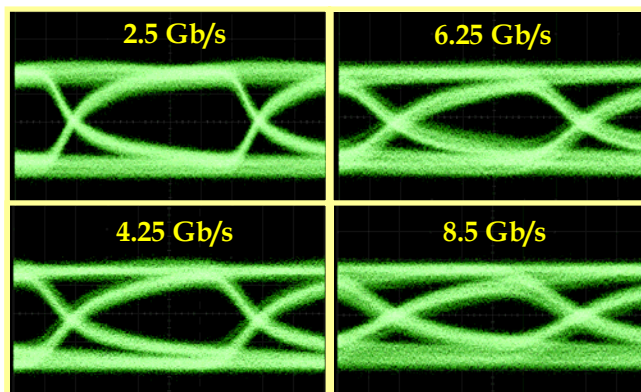


Fig. 7. Eye patterns (PRBS  $2^7-1$ ) measurements of the VPD at a bias of  $-1.0$  V. The detector demonstrated high sensitivity and low-noise photodetection up to a bit-rate of 8.5Gb/s. The low noise property of the detector can be clearly illustrated by the clean eye patterns.

Fig. 8(a) shows the total device capacitance measured as a function of the applied reverse voltages for different detector geometry. Obviously, elongating the detector length increases the capacitance due to a larger effective detector area, as predicted in equation (9). Moreover, in the presence of increased reverse bias, the capacitance drops drastically and nearly plateaus off at high voltage regime. This is attributed to the widening of the depletion layer width as the applied bias is raised. Further increase in the bias across the alternating p+ and n+ junctions would lead to a total depletion of the intrinsic-Ge region, which causes the device capacitance to reach a saturation level.

The theoretical modelling results of the RC-time constant and the transit-time bandwidth are plotted in Fig. 8(b). Reducing the depletion spacing enhances the transit-time bandwidth performance significantly, but it leads to a degraded RC-time bandwidth. To overcome this limitation, one could scale the detector length to achieve lower capacitance for bandwidth improvement.

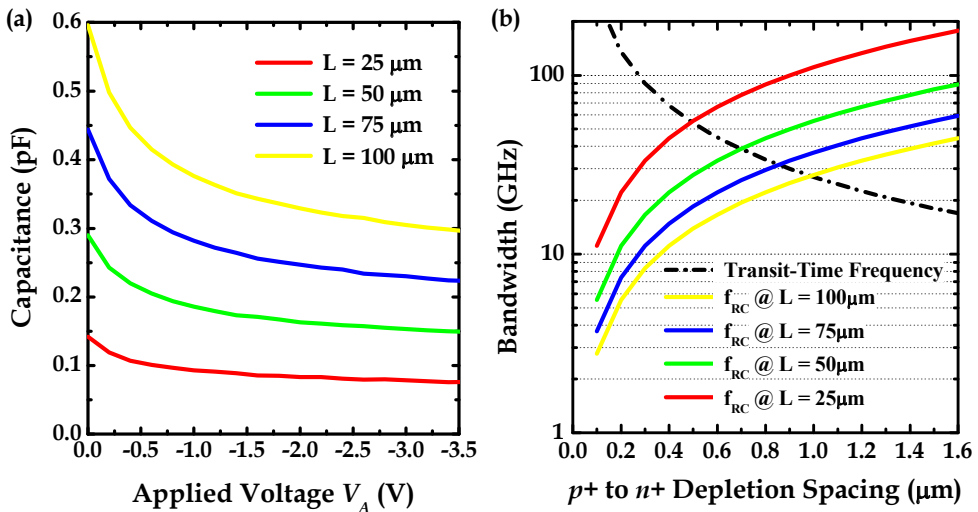


Fig. 8. (a) Measured capacitance as a function of applied voltage for Ge photodetector with various detector lengths. (b) Downscaling of detector length results in bandwidth enhancement due to a reduced device capacitance.

### 3.5 Impact of Band-Traps-Band Tunneling on Dark Current Generation

In order to gain insight into the leakage mechanism for the Ge detectors, an activation energy analysis of the dark current  $I_{Dark}$  was performed (Ang et al., 2009). In this analysis, the  $I_{Dark}$  can be modelled using the following functional form

$$I_{Dark} = BT^{3/2} e^{-E_a/kT} (e^{eV_a/2kT} - 1) \tag{12}$$

where T denotes the temperature,  $V_a$  the applied bias, and  $E_a$  the activation energy responsible for the leakage generation. Fig. 9(a) plots the bias dependence of dark current in a Ge p-i-n photodetector measured at increasing temperature range from 303K to 373K. As

can be observed from this figure, temperature has a significant impact on  $I_{Dark}$ . Increasing the operating temperature and the applied bias are found to result in a higher  $I_{Dark}$ . The applied bias  $V_A$  used in this measurement ranges from -1.5V to +0.2V.

A semi-log plot of  $I_{Dark}$  as a function of  $1/kT$  at various reverse bias voltages is shown in Fig. 9(b). A straight line fitting to this plot yields a gradient which corresponds to the activation energy  $E_a$ . At a fixed reversed bias of -0.5V, the extracted  $E_a$  is observed to be nearly half of the Ge bandgap energy  $E_g$ , which elucidates that the dark current mechanism is dominated by the Shockley-Read-Hall (SRH) process via deep levels in the Ge forbidden gap (Shockley & Read, 1952). This is not all unexpected as the large lattice mismatch between the two heterostructure materials could result in a Ge epitaxial film with high threading dislocation density. The existence of such defects has been shown to affect the effective carrier lifetime which causes an increase in the leakage current, as discussed earlier in Section 3.2.

Interestingly, the analysis also reveals a strong dependence of  $E_a$  on the electric field strength, as illustrated in Fig. 10(a). Increasing the field intensity across the depletion region is shown to result in a decreasing  $E_a$  responsible for the leakage generation. This in turn, contributes to an exponential increase in the dark current trend. The mechanism responsible for this is that electric field enlarges the band-bending which leads to an enhanced electrons and holes tunnelling from the resulting deep levels into the respective conduction and valence bands, thereby contributing to the dark current degradation. For instance, an increase in the electric field strength from 17kV/cm to 25kV/cm enhances the dark current from 0.27 $\mu$ A to 0.44 $\mu$ A, showing more than 60%  $I_{Dark}$  degradation.

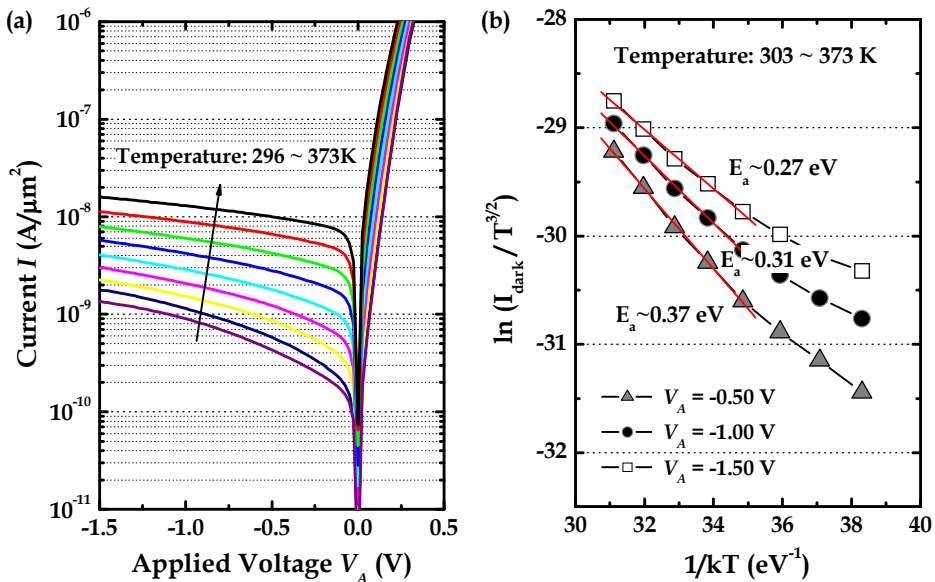


Fig. 9. (a) Plot of dark current characteristics as a function of applied bias for a Ge p-i-n photodetector with increasing temperature range from 303 K to 373 K. (b) An extraction of the activation energy for leakage generation as a function of applied bias.

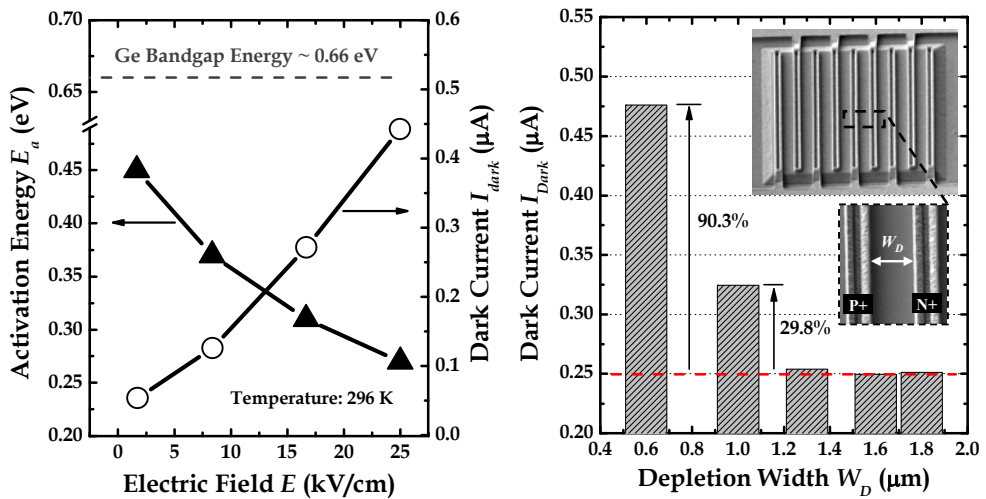


Fig. 10. (a) The activation energy  $E_a$  for leakage generation shows a strong dependence on the applied electric field, giving rise to a decreasing  $E_a$  trend with increasing field intensity. A reduced  $E_a$  at high field regime leads to an increased dark current generation. (b) Plot of dark current dependence on depletion width  $W_D$  of a Ge p-i-n photodetector. Scaling  $W_D$  leads to significantly higher dark current generation.

Such band-traps-band tunneling effect is observed to demonstrate a strong dependence on the depletion width  $W_D$  which separates the p+ and n+ metallurgical junctions. In this analysis, the area of the Ge detector is kept constant at  $23 \times 23 \mu\text{m}^2$  while the  $W_D$  is varied from 0.6~1.8  $\mu\text{m}$ . To avoid a difference in the contact area due to a variation of intrinsic Ge width, the metal geometry is also altered such that the total metal contact region is comparable for all designs. Note that a reduced  $W_D$  is often desirable from the perspective of enhancing the detector's bandwidth performance. Fig. 10(b) shows that an aggressive downsizing of  $W_D$  results in a significant dark current degradation. Specifically, a reduction of  $W_D$  from 1.3  $\mu\text{m}$  to 1.0  $\mu\text{m}$  increases the dark current density by ~29%, which is further aggravated to ~90% when  $W_D$  reaches 0.6  $\mu\text{m}$ .

The underlying mechanism responsible for such phenomenon can be explained using the band diagrams as shown in Fig. 11. When operated in the high field regime, enlarged band-bending results in a more prominent Ge bandgap narrowing for a detector with an aggressively scaled  $W_D$  [Fig. 11(a)]. As a consequence, the occurrence of electrons and holes tunnelling from the resulting mid-gap trap levels could be further enhanced in the presence of strong electric field, which accounts for the achievement of higher dark current over a detector with wide  $W_D$  [Fig. 11(b)]. It is also noteworthy to highlight that the dark current density begins to plateau for  $W_D > 1.3 \mu\text{m}$ , which implies that the influence of band-traps-band tunnelling on the leakage generation becomes relatively less prominent for wider  $W_D$ . This finding suggests that a design trade-off needs to be considered in the course of scaling  $W_D$  for enabling bandwidth enhancement as it would lead to a more pronounced dark current degradation.

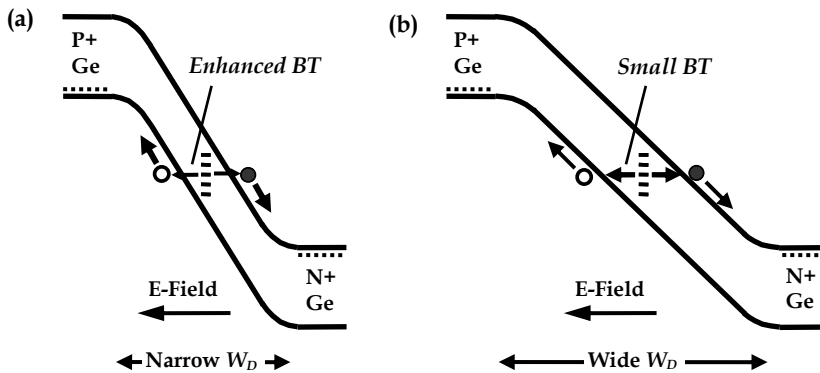


Fig. 11. Band diagrams illustrating the impact of scaling depletion width  $W_D$  on field-enhanced dark current generation. When operated at high field regime, enlarged band-bending results in a narrowing of Ge bandgap which enables electrons and holes tunnelling to occur via these defect centres. Such phenomenon is observed to become increasingly prominent for devices with (a) narrow  $W_D$  as compared to that with (b) wide  $W_D$ .

#### 4. Schottky Barrier Engineered Germanium MSM Photodetector

In another photodetector scheme, a metal-semiconductor-metal (MSM) structure was utilized to leverage on the advantage of low capacitance and ease of process integration. However, high dark current issue experienced in these detectors imposes much concern for the achievement of poor signal-to-noise (SNR) ratio. This drawback would be further aggravated when a narrow bandgap material such as Ge is employed, where high dark current is predominantly attributed to the low hole Schottky barrier height as a result of Fermi level pinning near the valence band edge. Recent experimental demonstration showed that Ge MSM photodetector with an integrated SOI rib waveguide exhibited high dark current on the order of  $150\mu\text{A}$  despite achieving impressive speed performance (Vivien et al., 2007). Such dark current level is way too high to be acceptable for high speed receiver design which typically tolerates a leakage current below  $1.0\mu\text{A}$ .

This chapter aims to deal with this problem through the application of novel approaches to suppress the leakage current in Ge MSM photodetector. The concepts are based upon Schottky barrier modulation through bandgap engineering as well as Fermi level de-pinning by segregating valence mending adsorbate at the metal/germanium interface.

##### 4.1 Schottky Barrier Modulation using Large Bandgap Material

The application of larger bandgap material for Schottky barrier modulation has been widely pursued to enable dark current suppression in Ge MSM photodetector. Oh et al. (2004) reported the fabrication of metal-Ge-metal photodetector featuring thin amorphous-Ge layer sandwiched between the metal and germanium interface to increase the Schottky barrier height. Using this approach, a substantial reduction of dark current by more than two orders of magnitude was achieved. Laih et al. (1998), on the other hand, adopted an amorphous-Si layer in a U-grooved metal-semiconductor-metal photodetector to enable

dark current suppression by more than three orders of magnitude. In this work, a novel crystalline silicon-carbon (Si:C) epilayer was proposed for modulating the Schottky barrier height in a Ge MSM photodetector with an integrated SOI micro-waveguide.

The fabrication process begins with an 8-inch silicon-on-insulator (SOI) substrate with (100) surface orientation. The SOI substrate features a silicon body thickness of  $\sim 250$  nm and a buried oxide thickness of  $\sim 1$   $\mu\text{m}$ . Si micro-waveguide was first formed by using anisotropic dry etching to achieve straight sidewall profile for enabling low propagation loss. After depositing a 120nm plasma enhanced chemical vapor deposition (PECVD) oxide as passivation layer, the Ge active regions were then patterned by reactive ion etching and cleaned with standard piranha solution (i.e. a mixture of sulfuric acid ( $\text{H}_2\text{SO}_4$ ) with hydrogen peroxide ( $\text{H}_2\text{O}_2$ ) for polymer removal. The wafers were subsequently cleaned with standard SC1 ( $\text{NH}_4\text{OH} : \text{H}_2\text{O}_2 : \text{H}_2\text{O}$ ) and then subjected to a HF-last wet cleaning for oxide removal prior to the selective epitaxial growth of Ge in an ultra high vacuum chemical vapor deposition (UHVCVD) system. The epitaxy growth started with an in-situ baking in  $\text{N}_2$  ambient at  $800^\circ\text{C}$  for native oxide removal and followed by the deposition of a  $\sim 5$  nm thin Si buffer at  $530^\circ\text{C}$ . A thin SiGe buffer layer was then deposited to have a gradual transition from pure Si to pure Ge at the hetero-interface. A Ge seed layer with a thickness of  $\sim 30$  nm was then grown using low temperature at  $370^\circ\text{C}$  before the growth of a  $\sim 300\text{nm}$  Ge epilayer at increased temperature. Precursor gases comprise of pure disilane  $\text{Si}_2\text{H}_6$  and diluted germane  $\text{GeH}_4$  (10%  $\text{GeH}_4$  : 90% Ar) were employed for the hetero-epitaxy growth of SiGe and Ge layers. The defects density within the Ge epilayer was measured to be on the order of  $10^7$   $\text{cm}^{-2}$  using etch-pit density (EPD) approach. Micro-Raman spectroscopy revealed a uniform distribution of residual tensile strain in the as-grown Ge film on Si substrate, which was attributed to the difference in the thermal expansion coefficient between Ge and Si during cooling.

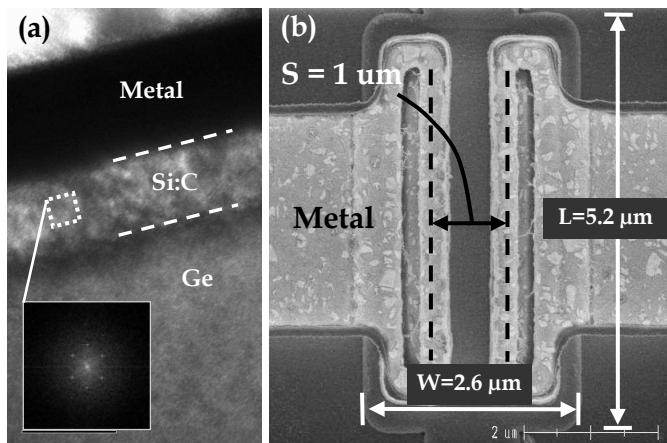


Fig. 12. (a) Silicon-carbon (Si:C) film is bi-dimensional and appears to be of good crystalline quality despite a substantial lattice mismatch between the Si:C barrier and the Ge epitaxial film. (b) SEM image of an evanescent coupled Ge-on-SOI MSM photodetector with an integrated Si micro-waveguide. The Ge detector features an effective device width  $W$  and length  $L$  of  $2.6\mu\text{m}$  and  $5.2\mu\text{m}$ , respectively. The metal contacts spacing  $S$  is  $\sim 1\mu\text{m}$ .

After contact hole patterning, a thin crystalline silicon-carbon (Si:C) epilayer of ~18nm was selectively deposited in the contact regions using disilane (Si<sub>2</sub>H<sub>6</sub>) and diluted monomethylsilane (SiH<sub>3</sub>CH<sub>3</sub>) precursor gases. Such an optimum Si:C thickness was chosen based on the considerations for acting as a good barrier layer to suppress leakage current while achieving low defects density at the heterojunction. Chlorine (Cl<sub>2</sub>) precursor gas was intermittently introduced to achieve selective epitaxial growth. The mole fraction of substitutional carbon incorporated in the Si:C film was measured to be ~1% based on the reciprocal lattice vector parameters obtained in X-Ray diffraction (Ang et al., 2007). Meanwhile, the total carbon concentration as obtained from SIMS analysis was found to be equal to ~1.3%, which means that around 0.3% of carbon was incorporated in the interstitial sites. Despite a substantial lattice mismatch, the Si:C layer is bi-dimensional and appears to be of good crystalline quality, as confirmed by the fast Fourier transform (FFT) diffractogram in Fig. 12(a). For comparison, Si:C epilayer was not deposited in a control sample. Metallization consisting of TaN/Al (250Å/6000Å) were subsequently deposited and patterned to complete the device fabrication. Fig. 12(b) shows the scanning electron microscopy (SEM) image of the evanescent coupled Ge-on-SOI MSM photodetector with an integrated Si micro-waveguide. The detector features an effective device length *L* and width *W* of 2.6 μm and 5.2 μm, respectively. The spacing *S* between the metal electrodes of the photodetector was lithographically defined to be ~1 μm.

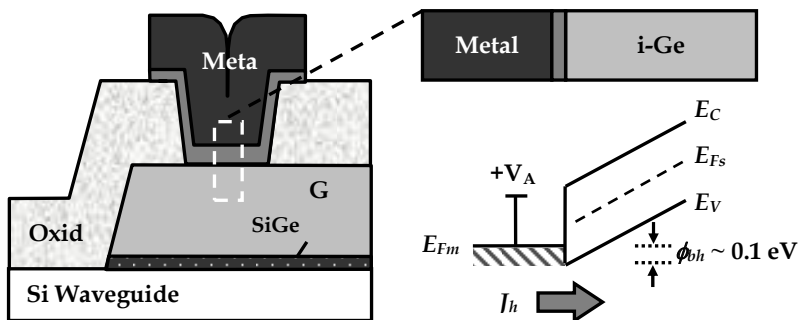


Fig. 13. Cross-sectional schematic of Ge photodetector featuring metal-semiconductor-metal configuration. Strong Fermi level pinning results in a low hole Schottky barrier height, which forms the root cause for the generation of high leakage current.

Fig. 13 depicts the cross-sectional schematic of a MSM configured Ge photodetector structure. Each photodetector can be represented by two back-to-back Schottky diodes. In the absence of the image force lowering effect, the Ge detection region between the metal electrodes will be totally depleted under high applied bias. The total dark current *J<sub>Total</sub>* flowing through the photodetector can then be described by the following expression

$$J_{Total} = J_p + J_n = A_p^* T^2 e^{-q\phi_{bh}/kT} + A_n^* T^2 e^{-q\phi_{be}/kT} \tag{13}$$

where *J<sub>p</sub>* (*J<sub>n</sub>*) is the hole (electron) current injected from the anode (cathode), and *A<sub>p</sub>*<sup>\*</sup> (*A<sub>n</sub>*<sup>\*</sup>) is the Richardson’s constant for hole (electron). Both the hole current and electron current are

observed to contribute to the dark current in the photodetector, which exhibit a strong dependence on the Schottky barrier for hole ( $\phi_{bh}$ ) and electron ( $\phi_{be}$ ), respectively. According to the Schottky-Mott theory on ideal metal-semiconductor system, the Schottky barrier height ( $\phi_B$ ) can be determined from the difference of the metal work function ( $\phi_m$ ) and the electron affinity of the semiconductor ( $\chi_S$ ), i.e.  $\phi_B = \phi_m - \chi_S$  (Tung, 2001). However, in practice, the presence of interface states has been shown to result in the Schottky barrier height less dependent on the metal work function. Strong Fermi level pinning feature of the metal/Ge or germanide/Ge junctions has been reported to contribute to high electron Schottky barrier  $\phi_{be}$ , and thus leading to low  $\phi_{bh} \sim 0.1\text{eV}$  (Dimoulas et al., 2006). As a result, hole injection is expected to dominate over electron injection in affecting the dark current of Ge MSM photodetector, as schematically illustrated in the band diagram of Fig. 13.

To circumvent this problem, a thin silicon-carbon (Si:C) Schottky barrier enhancement layer with bandgap energy  $E_g \sim 1.17\text{eV}$  (Soref, 1991) larger than that of Ge was inserted between the metal and Ge interface (Fig. 14). Due to Fermi level pinning away the valence band edge, an enhanced hole Schottky barrier height can be attained, as elucidated in the band diagram.

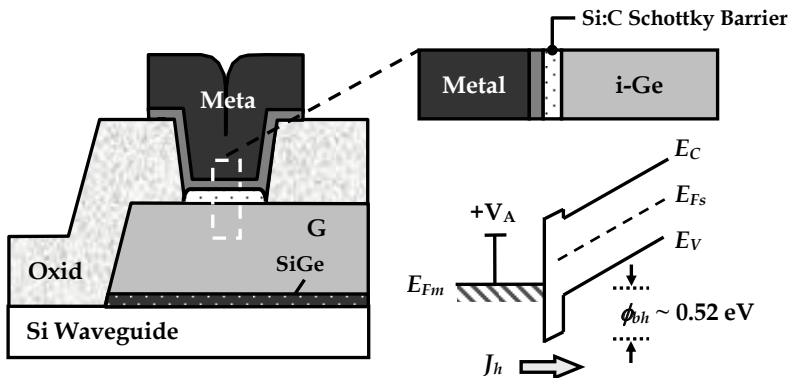


Fig. 14. Cross-sectional schematic of Ge MSM photodetector featuring silicon-carbon (Si:C) Schottky barrier enhancement layer. By inserting a large bandgap material between the metal and germanium interface, an enhanced hole Schottky barrier height can be achieved.

In order to accurately determine the enhancement of hole Schottky barrier due to the insertion of Si:C barrier layer, an activation energy measurement using low reverse bias voltage was employed. The temperature range used in the measurement varies from 303 K to 403 K, with an incremental increase of 10 K. Fig. 15 shows the Arrhenius plot for the extraction of activation energy under constant reverse bias  $V_R$  of 0.1V, according to the thermionic-emission model

$$\ln\left(\frac{I_R}{T^2}\right) = \ln(SA^*) - \frac{q\phi_{beff}}{kT} \quad (14)$$

where  $I_R$  denotes the reverse current,  $T$  the temperature,  $S$  the diode area,  $A^*$  the effective Richardson constant,  $q$  the elemental charge,  $k$  the Boltzmann constant, and  $\phi_{b,eff}$  the effective Schottky barrier that includes a contribution from the image force barrier lowering. The

temperature dependence of dark current was plotted in the inset of Fig. 15. An excellent fitting to the Arrhenius plot yields a gradient that is related to the Schottky barrier, showing a  $\phi_{bh}$  of  $\sim 0.52\text{eV}$  above the valence band edge.

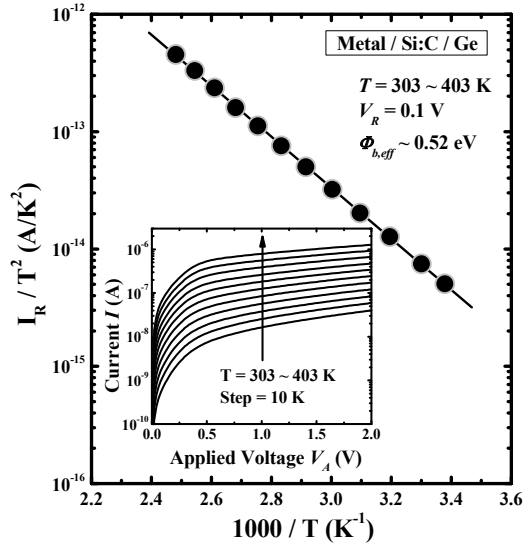


Fig. 15. Arrhenius plot for the extraction of activation energy under constant reverse bias of 0.1V according to the thermionic-emission model. The temperature dependence of dark current measurement was plotted in the inset.

Fig. 16(a) compares the dark current performance of both photodetectors with increasing reverse bias voltages. At a bias of 1.0V, high  $I_{Dark}$  of  $\sim 505.6\mu\text{A}$  ( $\sim 984.2\mu\text{A}$ ) was observed in a metal/Ge photodetector with a device width of  $5.2\mu\text{m}$  ( $10.2\mu\text{m}$ ). This  $I_{Dark}$  was substantially higher than the acceptable level of  $1\mu\text{A}$  for typical receiver application. However, through an insertion of Si:C barrier layer between the metal/Ge junction, a significant dark current reduction by more than 4 orders of magnitude was achieved due to an enhanced hole Schottky barrier. At a bias of 1.0V, the  $I_{Dark}$  was measured to be  $\sim 11.5\text{nA}$  ( $\sim 17.7\text{nA}$ ) for a device width of  $5.2\mu\text{m}$  ( $10.2\mu\text{m}$ ), showing the effectiveness of Si:C barrier layer in suppressing the dark current of MSM photodetector. Fig. 16(b) plots the photo-response characteristics of Ge MSM photodetector with Si:C Schottky barrier layer. The optical measurement was performed by injecting an incident photon with a wavelength of 1550nm into the Si waveguide using a multimode lensed fiber. The incident light power is  $\sim 150\mu\text{W}$ . High photo-current on the order of  $\sim 10^{-4}\text{A}$  was demonstrated, leading to good internal responsivity and quantum efficiency of  $\sim 530\text{mA/W}$  and  $\sim 42.4\%$ , respectively. These values were calculated based on an incident light power which excludes the fiber-to-waveguide coupling loss and the propagation loss components. Good signal-to-noise ratio of  $\sim 10^4$  was also demonstrated in the MSM photodetector with Si:C barrier layer.

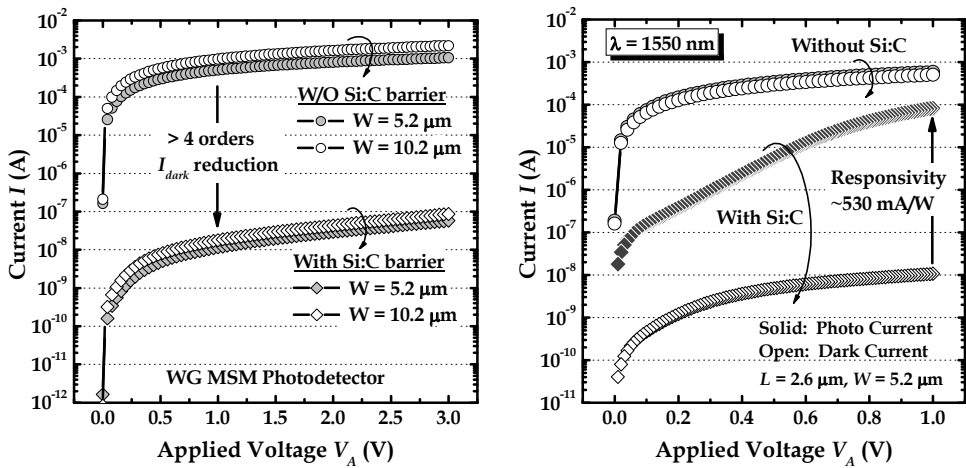


Fig. 16. (a) Dark current characteristics of Ge MSM photodetector with and without Si:C barrier layer. (b) Optical measurement results for both the detectors obtained at a photon wavelength of 1550nm.

A uniform spectral response of  $\sim 760 \text{ mA/W}$  was observed for wavelengths spanning from 1520-1560 nm, demonstrating an effective photo-detection for the entire C-band spectrum range [Fig. 17(a)]. In addition, the responsivities at wavelengths of 1570, 1590, and 1610 nm were measured to be 767, 602, and 290 mA/W, respectively, suggesting an extended potential for L-band optical photo-detection applications. Fig. 17(b) plots the frequency response measured at a wavelength of 1550nm, as obtained from the Fourier transform of an impulse response. A -3dB bandwidth of 12GHz was achieved for a low applied bias of 1.0V.

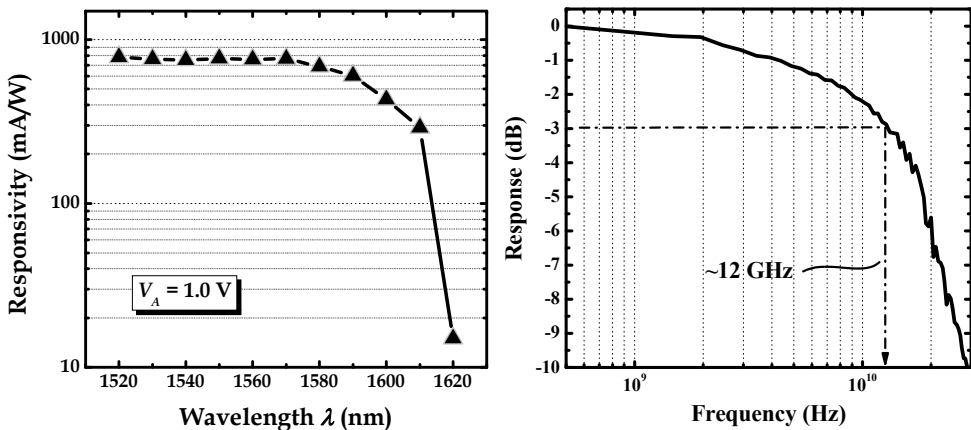


Fig. 17. (a) Spectral response as a function of wavelength for the novel MSM photodetector. (b) A -3dB bandwidth of  $\sim 12 \text{ GHz}$  was achieved at a photon wavelength of 1550nm.

## 4.2 Schottky Barrier Modulation via Valence Mending Adsorbate Segregation

In the preceding section, the adoption of bandgap engineering approach for Schottky barrier modulation has been shown to enable effective dark current suppression. In yet another approach, the application of dopant-segregation technique in metal-germanium-metal photodetectors has also been reported to enable substantial dark current reduction. By implanting and segregating arsenic (As) and boron (B) dopants at the NiGe/Ge junction in an alternating electrode pattern, Zang et al. (2008) showed that an impressive dark current suppression by ~3-4 orders of magnitude can be achieved. In this work, a novel concept in employing asymmetrical Schottky barriers through sulfur co-implantation and segregation at the NiGe/Ge interface was proposed and demonstrated. Introducing sulfur (S) at the germanide-semiconductor interface has been shown to allow Fermi level pinning close to the conduction band edge, which results in an increased hole Schottky barrier height. This in turn, enables the achievement of substantial dark current reduction by more than three orders of magnitude in a Ge MSM photodetector.

Starting silicon-on-insulator (SOI) substrate was employed for the fabrication of Ge MSM photodetector with sulfur-segregation. Field oxide isolation was first formed by the deposition of a 120 nm plasma enhanced chemical vapor deposition (PECVD) oxide and followed by the Ge active window patterning. Reactive ion etching was employed to open up the active window and then cleaned with standard piranha solution (i.e. a mixture of sulfuric acid ( $\text{H}_2\text{SO}_4$ ) with hydrogen peroxide ( $\text{H}_2\text{O}_2$ )) for polymer removal. Prior to the selective epitaxial growth of Ge in an ultra high vacuum chemical vapor deposition (UHVCVD) reactor, the wafers were subjected to standard SC1 ( $\text{NH}_4\text{OH} : \text{H}_2\text{O}_2 : \text{H}_2\text{O}$ ) clean and a HF-last wet process. Selective Ge epitaxy growth first started with an in-situ baking in  $\text{N}_2$  ambient at  $800^\circ\text{C}$  for native oxide removal and followed by the deposition of a ~5nm thin Si buffer at  $530^\circ\text{C}$ . A SiGe buffer layer of ~20nm was then deposited to have a gradual transition from pure Si to pure Ge at the interface. A low temperature growth at  $370^\circ\text{C}$  was subsequently employed to form a Ge seed layer of ~30nm before the high temperature Ge deposition at  $550^\circ\text{C}$ . Precursor gases comprise of pure disilane  $\text{Si}_2\text{H}_6$  and diluted germane  $\text{GeH}_4$  (10%  $\text{GeH}_4 : 90\% \text{Ar}$ ) were employed for the epitaxy growth of SiGe and Ge layers.

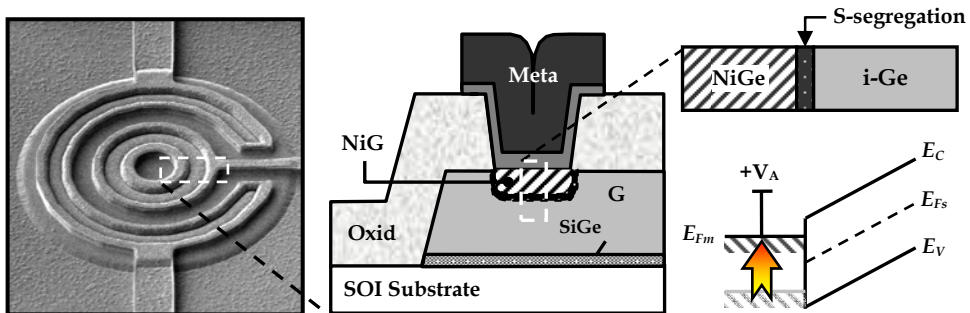


Fig. 18. Scanning electron microscopy (SEM) image of a Ge MSM photodetector with NiGe Schottky barrier. Co-implanting and segregating valence mending adsorbate such as sulfur at the NiGe/Ge interface leads to Fermi level de-pinning, which enables hole Schottky barrier enhancement.

On the device wafer, ion implantation of valence mending adsorbate such as sulfur (S) with a dose of  $1 \times 10^{15} \text{ cm}^{-2}$  and an implant energy of 10KeV was selectively performed on one side of the contact regions (Fig. 18). On the control wafer, sulfur implantation was not performed. After diluted HF clean, a thin nickel (Ni) film with a thickness of 30 nm was deposited on both wafers. Germanidation process was then performed using rapid thermal annealing (RTA) at a temperature of 500°C for 30 sec in  $\text{N}_2$  ambient to form nickel-monogermanide (NiGe) contacts. Diluted nitric acid ( $\text{HNO}_3:\text{H}_2\text{O}$ ) with a concentration of (1:10) was employed to remove the unreacted Ni after germanidation. Metallization consisting of tantalum-nitride/aluminium (250Å/6000Å) were subsequently deposited and patterned to complete the device fabrication. Fig. 18 shows the scanning electron microscopy (SEM) image of the completed Ge MSM photodetector featuring surface illumination scheme with an effective diameter of 32 $\mu\text{m}$ .

Fig. 19(a) shows the high resolution transmission electron microscopy (HRTEM) image of the NiGe/Ge junction, showing an excellent interface quality with an approximately uniform NiGe thickness of ~70nm. An X-ray diffraction (XRD) analysis confirmed the formation of a nickel-monogermanide (NiGe) phase after a RTA of 500°C for 30 sec. The achievement of low sheet resistance and contact resistance of metal-germanide are beneficial for enabling high-speed performance. Fig. 19(b) shows the secondary-ion-mass spectroscopy (SIMS) depth profile of a sulfur-segregated NiGe Schottky contact. While germanidation front proceeds, the implanted sulfur atoms are observed to pile up at the interface between the NiGe and the Ge junction. Due to this segregation, the dangling bonds at the NiGe/Ge interface can be effectively passivated, which results in the pinning of germanide Fermi level close to the conduction band edge. Hence, an increase in the hole Schottky barrier can be achieved for suppressing hole injection which forms the dominant component responsible for the high leakage current in Ge MSM photodetector.

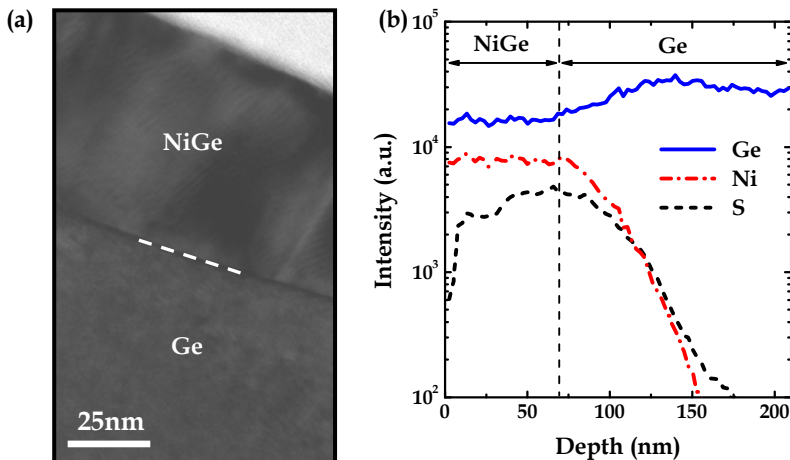


Fig. 19. (a) High resolution transmission electron microscopy (HRTEM) image showing the interface quality of the NiGe/Ge junction. (b) Secondary-ion-mass spectroscopy (SIMS) depth profile of a NiGe Schottky contact with sulfur-segregation.

Fig. 20 plots the room-temperature current-voltage (I-V) characteristics of the fabricated NiGe Schottky barrier Ge MSM photodetectors with and without sulfur-segregation. At an applied bias of 1.0V, high dark current ( $I_{\text{Dark}}$ ) on the order  $\sim 1.69\text{mA}$  was measured in a conventional photodetector without sulfur-segregation. Such high dark current performance is predominantly attributed to the large hole injection as a result of small hole Schottky barrier height  $\phi_{\text{bh}}$  of  $\sim 0.1\text{eV}$ . However, by introducing sulfur-segregation to passivate the dangling bonds at the NiGe/Ge interface, de-pinning of germanide Fermi level away the valence band edge was observed. This results in an increased hole Schottky barrier height ( $\phi_{\text{bh}}$ ) of  $\sim 0.49\text{eV}$ , leading to a significant dark current suppression by more than three orders of magnitude. For an applied bias of 1.0V, the  $I_{\text{Dark}}$  of Ge MSM photodetector with sulfur-segregation was measured to be merely  $\sim 0.42\mu\text{A}$ .

An extraction of Schottky barrier height based on the thermionic-emission model (Sze, 1981) further confirms the achievement of hole Schottky barrier modulation from  $\sim 0.1\text{eV}$  to  $\sim 0.49\text{eV}$  due to sulfur-segregation at the NiGe/Ge interface, consistent with that reported in (Ikeda et al., 2006). This leads to the formation of asymmetrical Schottky barriers in the Ge MSM photodetector, where high and low hole barrier height are achieved for contacts with and without sulfur-segregation, respectively (see band diagrams in Fig. 20).

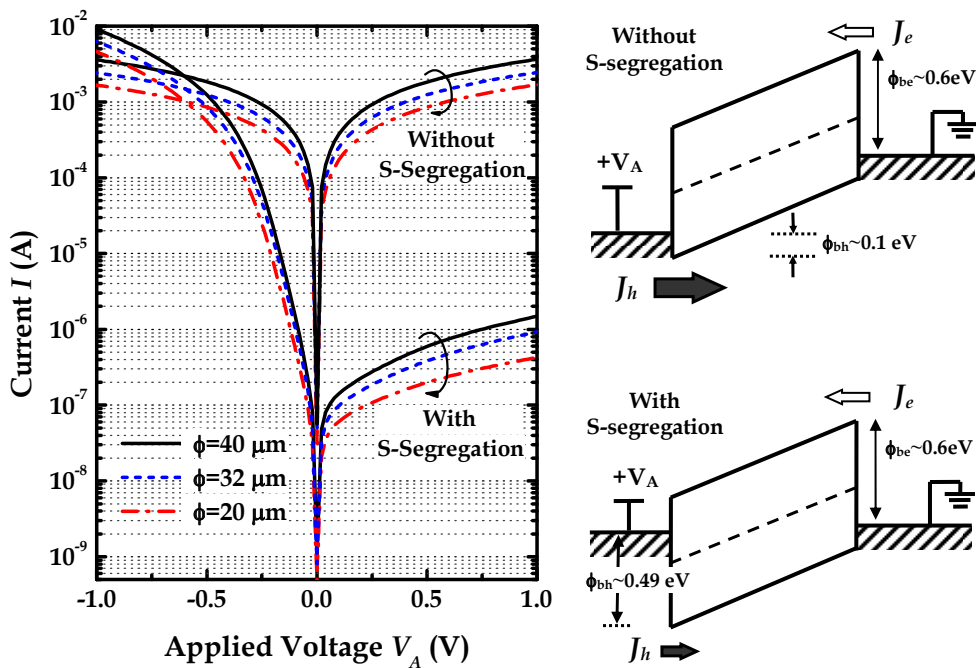


Fig. 20. Current-voltage (I-V) characteristics of the NiGe Schottky barrier photodetectors with and without sulfur-segregation. Significant reduction of dark current was achieved, predominantly attributed to the effective passivation of dangling bonds by the introduction of sulfur at the NiGe/Ge interface.

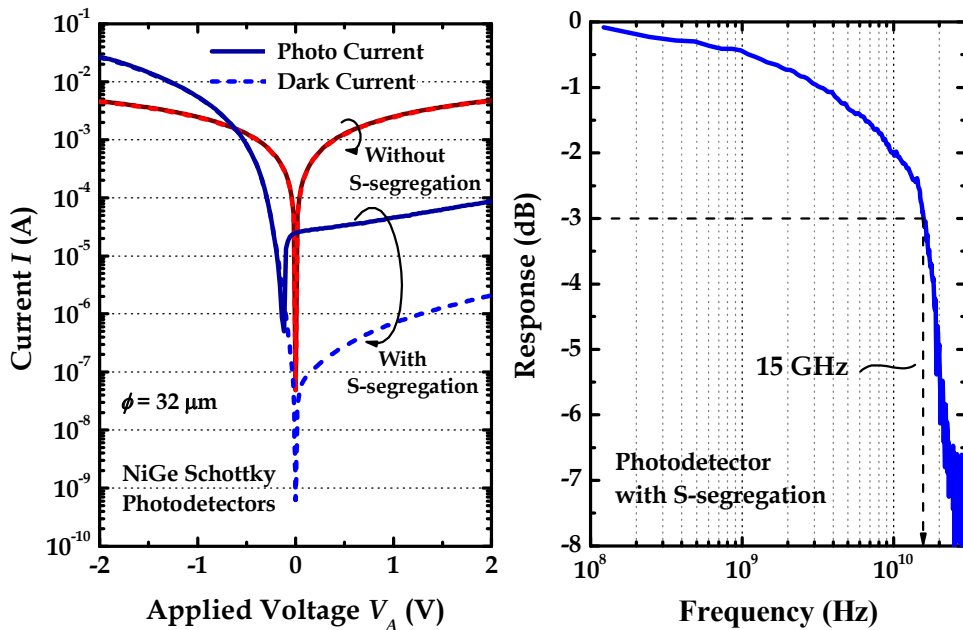


Fig. 21. (a) Photo-response characteristic of the Ge MSM photodetector with asymmetrical Schottky barriers. A responsivity of  $\sim 0.36\text{A/W}$  was achieved. (b) Normalized frequency response measured at a photon wavelength of  $1550\text{nm}$ . A  $-3\text{dB}$  bandwidth of  $\sim 15\text{GHz}$  was achieved for a low applied bias of  $1.0\text{V}$ .

Fig. 21(a) plots the photo-response characteristics of the NiGe Schottky photodetectors with and without sulfur-segregation. For a given applied bias of  $1.0\text{V}$ , good optical response of  $\sim 0.36\text{A/W}$  was achieved in a Schottky barrier engineered detector, which corresponds to a quantum efficiency of  $\sim 34\%$ . An appreciable signal-to-noise ratio of  $\sim 10^2$  was also observed in these devices. On the contrary, a conventional NiGe Schottky MSM photodetector without S-segregation showed a poor signal-to-noise ratio. This is attributed to the high dark current on the order of few mA, which renders it impractical for high sensitivity receiver application.

Fig. 22(b) shows the frequency response of the photodetectors measured under normal incidence illumination at a wavelength of  $1550\text{nm}$ , as obtained from the Fourier transform of an impulse response. A  $-3\text{dB}$  bandwidth of  $\sim 15\text{GHz}$  was achieved for a low applied bias of  $1.0\text{V}$ , showing comparable speed performance with that reported in (Vivien et al., 2007). On the contrary, the frequency response of a conventional photodetector could not be quantified for comparison as a result of its poor signal-to-noise ratio. Further enhancement in the responsivity and bandwidth performance could be achieved through a focused effort to optimize the Ge epilayer quality and the parasitic  $RC$  components. The adoption of smaller depletion layer width between the two metal electrodes could also contribute to a further bandwidth enhancement.

## 5. Ge/Si Avalanche Photodetector with High Gain-Bandwidth Product

Avalanche photodetectors (APD) are widely used in applications where high sensitivity is needed due to their internal carrier multiplication mechanism. Conventional APD receivers that are typically made of III-V compound semiconductors were shown to offer ~10dB sensitivity improvement over standard PIN receivers at a bit-rate of 10Gbs<sup>-1</sup>. However, the limited gain-bandwidth product in III-V based APD (typically in the range of 100~150GHz) makes it a less attractive option for high bit-rate applications. Recent advancements have revealed that Group-IV based semiconductors such as germanium (Ge) and silicon (Si) are attracting growing interests for the realization of high performance APDs due to their favorable absorption coefficient, low excess noise and high impact ionization rates (Webb et al., 1974) properties. Using CMOS-compatible process technology, Kang et al., (2008) reported the fabrication of monolithic Ge/Si APDs with impressive gain-bandwidth product and sensitivity of 340GHz and -28dBm, respectively. In this demonstration, blanket Ge epitaxy growth and etch-back approach were employed to form the optical absorption region. Silicon, on the other hand, is used to form the carrier multiplication region.

In this section, the design and fabrication of avalanche photodetector using Group-IV based heterostructure materials are discussed. The performance metrics such as gain-bandwidth product, carrier multiplication gain, dark current and breakdown voltage thermal coefficient are examined.

### 5.1 Ge/Si Avalanche Photodetector Design and Fabrication

The Ge/Si APD design used in this study features a separate-absorption-charge-multiplication (SACM) configuration in which germanium and silicon are employed for light absorption and carrier multiplication, respectively. Unlike the approach reported in (Kang et al., 2008), this work employs a low thermal budget selective epitaxy growth of Ge (SEG Ge) to form high quality optical absorption region. The adoption of SEG Ge growth not only eliminates process complexity associated with Ge etch-back, but also prevents early edge breakdown due to the formation of beveled sidewall.

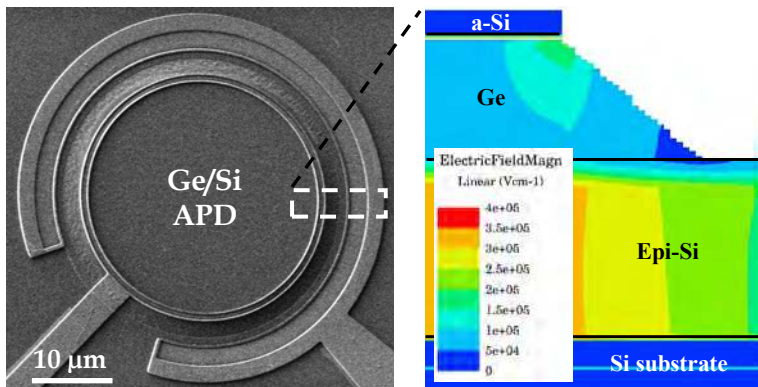


Fig. 22. Scanning electron microscopy (SEM) image of a surface illuminated Ge/Si avalanche photodetector. The simulated 2D electric field profile is plotted in the inset.

Fig. 22 shows the scanning electron microscopy (SEM) image of the Ge/Si APD demonstrated in this work. The device fabrication started with 8-inch p-type bulk Si wafers. Ion implantation employing arsenic dopants with a relatively high dose ( $1 \times 10^{15} \text{cm}^{-2}$ ) was performed to form n-type contact layer with low series resistance. Blanket Si epitaxial layer with a thickness of  $0.6 \mu\text{m}$  was grown at a temperature of  $640^\circ\text{C}$  using an ultra high vacuum chemical vapor deposition (UHVCVD) reactor. This was followed by the p-type charge layer formation by implanting boron at  $1.5 \times 10^{12} \text{cm}^{-2}$  onto the epi-Si surface. Circular mesas of diameter  $28 \mu\text{m}$  are patterned by anisotropic dry etching into the epi-Si layer. Oxide window was formed using a combination of dry etch and followed by wet etch approach to preserve the top Si surface quality from possible damage by the reactive ion etching process. Hetero-epitaxy of Ge was then selectively grown in an UHVCVD epitaxy reactor. The selective Ge epitaxy process commenced with the deposition of a low temperature pseudo-graded silicon-germanium buffer ( $\sim 20 \text{nm}$ ) and followed by a Ge seed layer with a thickness of  $\sim 30 \text{nm}$ . The temperature was then increased to  $\sim 550^\circ\text{C}$  to complete the Ge growth using cyclical deposition and etch back approach. The top and sidewalls of the epi-Ge are then covered with  $100 \text{nm}$  of amorphous Si (a-Si) for passivation. The a-Si layer was implanted with high dose boron and dopants are activated at  $750^\circ\text{C}$  to form p-type ohmic contact. Nickel silicidation of the *p* and *n* contacts was done to further reduce the contact resistance. The fabrication process was completed after the formation of aluminium interconnects and an anti-reflective coating (ARC) layer.

The 2D contour map of the electric field profile as obtained using commercial MEDICI simulator is plotted in the inset of Fig. 22. The formation of bevelled Ge sidewall ( $\sim 20^\circ$ ) is observed to contribute to a reduced electric field strength at the mesa edge which is advantageous in preventing early edge breakdown. This is true for both the base of the Ge absorption layer and the edge of the epi-Si layer. This eliminates the need for a floating guard ring to reduce the surface electric field strength at the silicon/insulator interface to prevent premature breakdown along the device perimeter (Kang et al., 2008).

## 5.2 Performance Metric of Ge/Si APD

Fig. 23 plots the current-voltage (I-V) characteristics of a Ge/Si APD with a cross-sectional diameter of  $28 \mu\text{m}$  measured under dark and illumination conditions. Using SACM configuration, the detector was observed to exhibit a typical rectifying characteristic at room temperature. Under low applied bias of less than  $-10 \text{V}$ , the space charge region extends primarily within the Si multiplication layer. This results in a relatively insignificant dark current on the order of few nano-ampere (nA). Further increase in the applied reverse bias causes a widening of the depletion region into the Ge absorption layer. When this occurs, the dark current begins to increase rapidly due to trap-assisted generation within the depletion region as governed by the Shockley-Read-Hall (SRH) process. At  $-15 \text{V}$ , the Ge absorption layer was observed to be fully depleted, which indicates the occurrence of punchthrough phenomenon. The dark current density at punchthrough was measured to be  $\sim 8.5 \text{mA/cm}^2$  but increases to  $\sim 320 \text{mA/cm}^2$  at 90% of the breakdown voltage. Such dark current level is competitive to that achieved in a state-of-the-art Ge p-i-n photodetector reported in the literature (Morse et al., 2006). This shows that enlarged electric field strength does not lead to a severe dark current degradation despite the possibility to experience defects-assisted tunneling current (Moll, 1964).

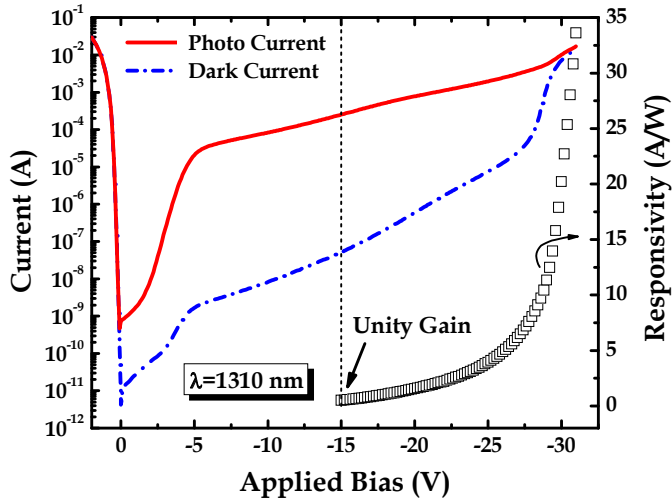


Fig. 23. Current-voltage characteristics of a Ge/Si APD with a cross-sectional diameter of 28μm. Due to an internal carrier multiplication gain, very impressive responsivity performance was demonstrated at a wavelength of 1310nm.

Normal incidence illumination with a wavelength of 1310nm was performed to extract the responsivity performance of the Ge/Si APD. Using conventional Ge p-i-n detector as a reference, the primary responsivity was measured to be ~0.51A/W, which corresponds to a quantum efficiency of ~48.2%. This is slightly smaller than the expected responsivity of 0.55A/W by assuming that the Ge absorption coefficient is 0.706μm<sup>-1</sup> at 1310nm. A possible reason to explain this discrepancy is the occurrence of Ge-Si inter-diffusion along the hetero-interfaces which reduces the absorption coefficient. This is in good agreement with the Ge/Si APD responsivity at unity gain. Further increase in the applied bias causes the responsivity to rise rapidly. When operated at 90% of the breakdown voltage, a responsivity as high as ~4.2A/W was achieved in the APD (Fig. 23). Such high photoresponse is possible due to avalanche effects which enable carrier multiplication to take place within the Si multiplication layer.

By normalizing the APD's responsivity to the primary responsivity of a reference p-i-n detector, the multiplication gain factor can be calculated. Fig. 24 plots the dependence of multiplication gain (*M*) on the applied reverse bias of the Ge/Si APD at room temperature. Unity gain (*M*=1) was observed to occur at punchthrough voltage of -15V. With a further increase in the applied bias beyond punchthrough, the multiplication gain increases rapidly and could reach a value of ~8.2 at 90% of breakdown voltage.

However, the achievement of large multiplication gain could potentially impose a major concern for a degraded dark current which affects the APD receiver sensitivity. For a Ge/Si APD, the total measured dark current (*I*<sub>Total</sub>) can be expressed in terms of the multiplied dark current (*I*<sub>multiplied</sub>) and the unmultiplied dark current (*I*<sub>unmultiplied</sub>) using

$$I_{Total} = I_{unmultiplied} + I_{multiplied} \cdot M \tag{15}$$

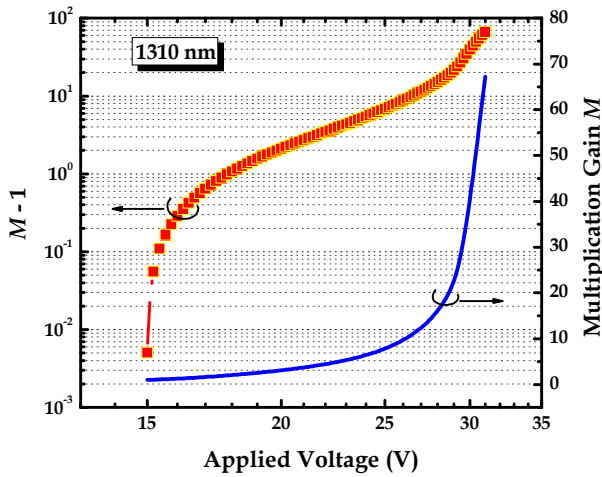


Fig. 24. The dependence of carrier multiplication gain on applied voltages. Higher gain is achieved with increasing biases.

As expected, increasing the carrier multiplication gain leads to higher dark current density, as shown in Fig. 25. At room temperature, the dark current is increased by one order of magnitude when the gain is increased from  $M=5$  to  $M=25$ . Moreover, the dark current also demonstrates a strong dependence on temperature. Increasing the operating temperature from  $23^{\circ}\text{C}$  to  $90^{\circ}\text{C}$  has been shown to result in more than one order of magnitude increase in the dark current at a multiplication gain of 10.

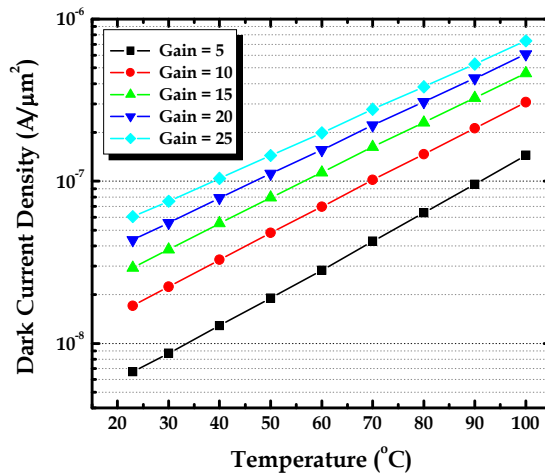


Fig. 25. The temperature dependence on dark current as a function of carrier multiplication gain. Both an increase in the multiplication gain and temperature results in a higher dark current density in a Ge/Si APD.

Fig. 26 plots the dependence of breakdown voltage ( $V_{bd}$ ) on the operating temperature of a Ge/Si APD. The measurements are performed over a temperature range from 273K to 333K. A linear fitting to this plot yields a gradient which corresponds to the breakdown voltage thermal coefficient ( $\delta$ ) as defined by

$$\delta = \frac{\Delta V_{bd}}{\Delta T} \quad (16)$$

The extraction shows a  $\delta$  value of 15mV/K, which is merely less than half of that obtained in a typical III-V based APD made of InP/InGaAs compound semiconductors (Ma et al., 1995). This makes Si a preferred material to meet the stringent requirement for thermal stability in APD receiver as it exhibits the least temperature sensitivity for breakdown voltage.

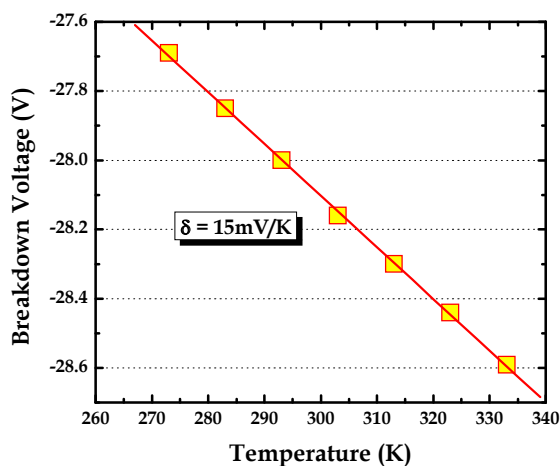


Fig. 26. The temperature dependence of breakdown voltage in Ge/Si APD. A small breakdown voltage thermal coefficient of 15mV/K was achieved.

The electrical -3dB bandwidth of the Ge/Si APD was measured using network analyzer at a wavelength of 1310nm. The frequency response was obtained from an APD with a diameter of 28 $\mu$ m. When the device is operated at low multiplication gain ( $M=10$ ), a maximum -3dB bandwidth of ~7.5GHz was achieved, where RC time constant is found to be the dominant factor limiting the speed performance. This is lower than the expected theoretical bandwidth of 10GHz, which could possibly be due to parasitic effects such as high series resistance and capacitance between the metal pads. This is true as the total capacitance was measured to be ~230fF, in which 180fF was contributed by the metal pads while 50fF originates from the detector's junction capacitance. When operated in the high gain region, a slight decrease in the APD bandwidth is observed, which is predominantly attributed to the avalanche build-up time effect. For a multiplication gain of 23, a lower -3dB bandwidth of ~7.4GHz is achieved. This gives rise to a resulting gain-bandwidth product of 180GHz for the Ge/Si APD demonstrated in this work. Moreover, a CMOS TIA packaged Ge/Si APD achieved a very impressive sensitivity of -27.5dBm at a bit-rate of 10Gb/s, showing comparable performance to that of III-V based APD. Fig. 27 depicts a summary that

benchmarks the gain-bandwidth product of III-V based and Si-based APDs reported in the literature. Clearly, Si-based APDs have out-performed III-V based APDs in terms of the gain-bandwidth performance, which makes it an extremely attractive option for 1.31 $\mu\text{m}$  fiber-link applications.

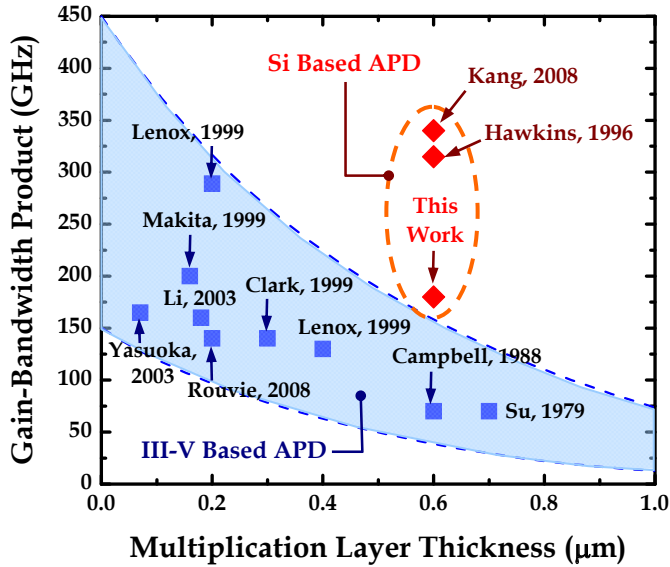


Fig. 27. A summary showing the benchmark of gain-bandwidth products as a function of multiplication layer thickness for both III-V based and silicon-based APDs.

## 6. Conclusion

In this chapter, the progress and development of Ge-based photodetector technologies for optical communication applications are discussed. To enable the realization of silicon photonics interconnect solutions, the development of Ge-on-Si hetero-epitaxy process that is compatible with existing CMOS fabrication technology is extremely important. Due to a large lattice mismatch between the two hetero-structure materials, high threading dislocations density within the Ge epilayer is not all unexpected. Various approaches proposed to overcome this technological challenge are discussed. Using low temperature pseudo-graded SiGe buffer engineering, low dislocations density on the order of  $\sim 10^7\text{cm}^{-2}$  has been achieved without the need to undergo additional high temperature annealing step. By leveraging on such high quality hetero-epitaxy platform, various state-of-the-art Ge-based photodetector schemes are proposed and demonstrated in this work. This includes the design and fabrication of Ge *p-i-n* photodetector with an integrated SOI micro-waveguide. The performance metrics of this detector are systematically discussed. Very impressive responsivity of  $\sim 0.9\text{A/W}$  (at 1550nm) and dark current density of  $\sim 0.7\text{nA}/\mu\text{m}^2$  are demonstrated, along with the achievement of high bandwidth performance of  $>11\text{GHz}$ .

Parameter	Ge PIN PD	Ge MSM PD	Ge/Si APD
<b>Responsivity</b> ( $\lambda = 1550 \text{ nm}$ )	Waveguided • 0.90 A/W Normal Incidence • 0.45 A/W	Waveguided • 0.76 A/W Normal Incidence • 0.36 A/W	Normal Incidence • > 5.0 A/W (Gain ~ 10)
<b>-3dB Bandwidth</b>	Waveguided • > 11 GHz Normal Incidence • > 9 GHz	Waveguided • > 15 GHz Normal Incidence • > 12 GHz	Normal Incidence • 7.5 GHz (G=10) • 7.4 GHz (G=23)
<b>Gain-Bandwidth Product</b>	• N.A.	• N.A.	• 180 GHz
<b>Dark Current</b>	Waveguided • 0.7 nA/ $\mu\text{m}^2$ Normal Incidence • 1 nA/ $\mu\text{m}^2$	Waveguided • 0.9 nA/ $\mu\text{m}^2$ Normal Incidence • 1.1 nA/ $\mu\text{m}^2$	Normal Incidence • 3.2 nA/ $\mu\text{m}^2$ (@ 90% $V_b$ )

Table 1. A summary showing the performance metrics of the various state-of-the-art Ge-based photodetectors developed in this work.

In addition, this chapter also deals with the high leakage current issue commonly seen in Ge photodetectors featuring metal-semiconductor-metal (MSM) configuration. Approaches reported in the literature to circumvent this problem are reviewed. By employing bandgap engineering approach through the use of new silicon-carbon Schottky barrier enhancement layer, significant dark current suppression by more than four orders of magnitude has been achieved. Novel concept in employing valence mending adsorbate segregation to de-pin the germanide Fermi level away the valence band edge is also proposed and demonstrated. The mechanism responsible for the hole Schottky barrier enhancement is elucidated.

Recent technological breakthrough in employing all Group-IV based materials for the realization of high performance Ge/Si avalanche photodetector is discussed. Using separate-absorption-charge-multiplication (SACM) configuration design, the Ge/Si APD demonstrated excellent gain-bandwidth product, large carrier multiplication gain, and low breakdown voltage thermal coefficient. These performances have been shown to be comparable, if not better, to the commercially available III-V based APDs.

Table 1 outlines a summary which compares the performance metrics of the various photodetectors demonstrated in this work. Each detector scheme has its own merits which can be leveraged to meet the stringent requirements of future integrated photonics circuits. A successful implementation of these state-of-the-art Ge-based photodetector technologies is poised to become an enabling technology to realize on-chip optical interconnects for next-generation high bandwidth computing applications.

## 7. References

- Ang K.-W., Chui K.-J., Tung C.-H., Balasubramanian N., Samudra G. S., & Yeo Y.-C. (2007). Performance enhancement in uniaxial strained silicon-on-insulator N-MOSFETs featuring silicon-carbon source/drain regions, *IEEE Transactions on Electron Devices*, Vol. 54, No. 11, pp. 2910–2917.
- Ang K.-W., Zhu S., Yu M., Lo G.-Q., & Kwong D.-L. (2008). High Performance Waveguided Ge-on-SOI metal-semiconductor-metal photodetectors with novel silicon-carbon (Si:C) Schottky barrier enhancement layer, *IEEE Photonics Technology Letters*, Vol. 20, No. 9, pp. 754–756.
- Ang K.-W., Yu M.-B., Zhu S.-Y., Chua K.-T., Lo G.-Q., & Kwong D.-L. (2008). Novel NiGe MSM photodetector featuring asymmetrical Schottky barriers using sulfur co-implantation and segregation, *IEEE Electron Device Letters*, Vol. 29, No. 7, pp. 704–707.
- Ang K.-W., Zhu S. Y., Wang J., Chua K. T., Yu M. B., Lo G. Q., & Kwong D. L. (2008). Novel silicon-carbon (Si:C) Schottky barrier enhancement layer for dark current suppression in Ge-on-SOI MSM photodetectors, *IEEE Electron Device Letters*, Vol. 29, No. 7, pp. 708–710.
- Ang K.-W., Ng J. W., Lo G.-Q., & Kwong D.-L. (2009). Impact of field-enhanced band-traps-band tunneling on the dark current generation in germanium p-i-n photodetector, *Applied Physics Letters*, Vol. 94, No. 22, pp. 223515–223517.
- Ang K.-W., Liow T.-Y., Yu M.-B., Fang Q., Song J., Lo G.-Q., & Kwong D.-L. (2010). Low thermal budget monolithic integration of evanescent coupled Ge-on-SOI photodetector on Si-CMOS platform, to appear in *IEEE Journal of Selected Topics in Quantum Electronics*, Vol. 14, In Press.
- Beals M., Michel J., Liu J. F., Ahn D. H., Sparacin D., Sun R., Hong C. Y., Kimerling L. C., Pomerene A., Carothers D., Beattie J., Kopa A., Apsel A., Rasras M. S., Gill D. M., Patel S. S., Tu K. Y., Chen Y. K., & White A. E. (2008). Process flow innovations for photonic device integration in CMOS, *Proceedings of SPIE*, Vol. 6898, p. 689804.
- Campbell J. C., Tsang W. T., Qua G. J., & Johnson B. C. (1988). High-speed InP/InGaAsP/InGaAs avalanche photodiodes grown by chemical beam epitaxy, *IEEE Journal of Quantum Electronics*, Vol. 24, No. XX, pp. 496–500.
- Clark W. R. (1999). Reliable, high gain-bandwidth product InGaAs/InP avalanche photodiodes for 10 Gbs<sup>-1</sup> receivers, *Proc. Opt. Fiber Comm.*, Vol. 1, pp. 96–98.
- Colace L., Masini G., & Assanto G. (1999). Ge-on-Si approaches to the detection of near-infrared light, *IEEE Journal of Quantum Electronics*, Vol. 35, No. 12, pp. 1843–1852.
- Dimoulas A., Tsiapas P., Sotiropoulos A., & Evangelou E. K. (2006). Fermi-level pinning and charge neutrality level in germanium, *Applied Physics Letters*, Vol. 89, No. 25, pp. 252110–252112.
- Gunn C. (2006). CMOS photonics for high-speed interconnects, *IEEE Micro*, Vol. 26, No. 2, pp. 58–66.
- Hartmann J. M., Abbadie A., Papon A. M., Holliger P., Rolland G., Billon T., Fedeli J. M., Rouviere M., Vivien L., & Laval S. (2004). Reduced pressure-chemical vapor deposition of Ge thick layers on Si(001) for 1.3–1.55- $\mu\text{m}$  photodetection, *Journal of Applied Physics*, Vol. 95, No. 10, pp. 5905–5913.

- Hawkins A. R., Wu W., Abraham P., Streubel K., & Bowers J. E. (1996). High gain-bandwidth-product silicon heterointerface photodetector, *Applied Physics Letters*, Vol. 70, No. 3, pp. 303-305.
- Huang Z., Oh J., & Campbell J. C. (2004). Back-side-illuminated high-speed Ge photodetector fabricated on Si substrate using thin SiGe buffer layers, *Applied Physics Letters*, Vol. 85, No. 15, pp. 3286-3288.
- Ikeda K., Yamashita Y., Sugiyama N., Taoka N., & Takagi S.-I. (2006). Modulation of NiGe/Ge Schottky barrier height by sulfur segregation during Ni germanidation, *Applied Physics Letters*, Vol. 88, No. 15, pp. 152115-152117.
- Kang Y., Liu H.-D., Morse M., Paniccia M. J., Zadka M., Litski S., Sarid G., Pauchard A., Kuo Y.-H., Chen H.-W., Zaoui W. S., Bowers J. E., Beling A., McIntosh D. C., Zheng X., & Campbell J. C. (2008). Monolithic germanium/silicon avalanche photodiodes with 340 GHz gain-bandwidth product, *Nature Photonics*, Vol. 3, No. 1, pp. 59-63.
- Kimerling L. C., Ahn D., Apsel A. B., Beals M., Carothers D., Chen Y. K., Conway T., Gill D. M., Grove M., Hong C.-Y., Lipson M., Liu J., Michel J., Pan D., Patel S. S., Pomerene A. T., Rasras M., Sparacin D. K., Tu K.-Y., White A. E., & Wong C. W. (2006). Electronic-photonic integrated circuits on the CMOS platform, *Proceedings of SPIE*, Vol. 6125, p. 12502.
- Laih L.-H., Chang T.-C., Chen Y.-A., Tsay W.-C., & Hong J.-W. (1998). Characteristics of MSM photodetectors with trench electrodes on P-type Si wafer, *IEEE Transactions on Electron Devices*, Vol. 45, No. 9, pp. 2018-2023.
- Lenox C., Nie H., Yuan P., Kinsey G., Homles A. L., Streetman B. G., & Campbell J. C. (1999). Resonant-cavity InGaAs-InAlAs avalanche photodiodes with gain-bandwidth product of 290 GHz, *IEEE Photonics Technology Letters*, Vol. 11, No. 9, pp. 1162-1164.
- Li N., Sidhu R., Li X. W., Ma F., Zheng X. G., Wang S. L., Karve G., Demiguel S., Holmes A. L., & Campbell J. C. (2003). InGaAs/InAlAs avalanche photodiode with undepleted absorber, *Applied Physics Letters*, Vol. 82, No. 13, pp. 2175-2177.
- Luan H.-C., Lim D. R., Lee K. K., Chen K. M., Sandland J. G., Wada K., & Kimerling L. C. (1999). High-quality Ge epilayers on Si with low threading-dislocation densities, *Applied Physics Letters*, Vol. 75, No. 19, pp. 2909-2911.
- Ma C. L. F., Dean M. J., Tarof L. E., & Yu J. C. H. (1995). Temperature dependence of breakdown voltages in separate absorption, grading, charge, and multiplication InP/InGaAs avalanche photodiodes, *IEEE Transactions on Electron Devices*, Vol. 42, No. 5, pp. 810-818.
- Makita K., Nakata T., Watanabe I. & Taguchi K. (1999). High-frequency response limitation of high performance InAlGaAs/InAlAs superlattice avalanche photodiodes, *Electron. Lett.*, Vol. 35, No. 25, pp. 2228-2229.
- Mamor M., Perrossier J.-L., Aubry-Fortuna V., Meyer F., Bouchier D., Bodnar S., & Regolini J. L. (1997). Fermi-level pinning in Schottky diodes on IV-IV semiconductors: effect of Ge and C incorporation, *Thin Solid Films*, Vol. 294, No. 1/2, p. 141-144.
- Moll J. L. (1964). *Physics of semiconductors*, McGraw-Hill, New York.
- Morse M., Dosunmu O., Sarid G., & Chetrit Y. (2006). Performance of Ge-on-Si p-i-n Photodetectors for Standard Receiver Modules, *Proceeding of SiGe and Ge: Materials, Processing, and Devices*, Vol. 3, No. 7, pp. 75-84.

- Oh J., Banerjee S. K., & Campbell J. C. (2004). Metal-germanium-metal photodetectors on heteroepitaxial Ge-on-Si with amorphous Ge Schottky barrier enhancement layers, *IEEE Photonics Technology Letters*, Vol. 16, No. 2, pp. 581-583.
- Rouvie A., Carpentier D., Lagay N., Decobert J., Pommereau F., & Achouche M. (2008). High gain bandwidth product over 140 GHz planar junction AlInAs avalanche photodiodes, *IEEE Photonics Technology Letters*, Vol. 20, No. 5-8, pp. 455-457.
- Shockley W. & Read T. W. (1952). Statistics of the recombinations of holes and electrons. *Physical Review*, Vol. 87, No. 5, pp. 835-842.
- Soref R. A. (1991). Optical band gap of the ternary semiconductor  $\text{Si}_{1-x-y}\text{Ge}_x\text{C}_y$ , *Journal of Applied Physics*, Vol. 70, No. 4, pp. 2470-2472.
- Soref R. (2006). The past, present, and future of silicon photonics, *IEEE Journal of Selected Topics in Quantum Electronics*, Vol. 12, No. 6, pp. 1678-1687.
- Su Y. K., Chang C. Y., & Wu T. S. (1979). Temperature dependent characteristics of a PIN avalanche photodiode (APD) in Ge, Si and GeAs, *Opt. Quant. Electron.*, Vol. 11, No. 2, pp. 109-117.
- Sze S. M. (1981). *Physics of semiconductor devices*, Wiley, New York.
- Tung R. T. (2001). Recent advances in Schottky barrier concepts, *Mater. Sci. Eng.*, Vol. 35, No. 1, pp. 1-138.
- Vivien L., Rouvière M., Fédéli J.-M., Morini, D. M., Damlencourt J.-F., Mangeney J., Crozat P., Melhaoui L. E., Cassan E., Roux X. L., Pascal D., & Laval S. (2007). High speed and high responsivity germanium photodetector integrated in a Silicon-On-Insulator microwaveguide, *Optics Express*, Vol. 15, No. 15, pp. 9843-9848.
- Wada K., Luan H. C., Lim D. R. C., & Kimerling L. C. (2002). On-chip interconnection beyond semiconductor roadmap-Silicon microphotonics, *Proceedings of SPIE*, Vol. 4870, pp. 437-443.
- Webb P. P., McIntyre R. J., & Conradi J. (1974). Properties of avalanche photodiodes, *RCA Review*, Vol. 35, pp. 234-278.
- Yasuoka N., Kuwatsuka H., & Makiuchi M. (2003). Large multiplication-bandwidth products in APDs with a thin InP multiplication layer, *Proc. 16th IEEE Annual Meeting of LEOS*, pp. 999-1000.
- Yin T., Cohen R., Morse M. M., Sarid G., Chetrit Y., Rubin D., & Paniccia M. J. (2007). 31GHz Ge n-i-p waveguide photodetectors on Silicon-on-Insulator substrate, *Optics Express*, Vol. 15, No. 21, pp. 13965-13971.
- Zang H., Lee S. J., Loh W. Y., Wang J., Chua K. T., Yu M. B., Cho B. J., Lo G. Q., & Kwong D. L. (2008). Dark-current suppression in metal-germanium-metal photodetectors through dopant-segregation in NiGe-Schottky barrier, *IEEE Electron Device Letters*, Vol. 29, No. 2, pp. 161-164.



## **Semiconductor Technologies**

Edited by Jan Grym

ISBN 978-953-307-080-3

Hard cover, 462 pages

**Publisher** InTech

**Published online** 01, April, 2010

**Published in print edition** April, 2010

Semiconductor technologies continue to evolve and amaze us. New materials, new structures, new manufacturing tools, and new advancements in modelling and simulation form a breeding ground for novel high performance electronic and photonic devices. This book covers all aspects of semiconductor technology concerning materials, technological processes, and devices, including their modelling, design, integration, and manufacturing.

### **How to reference**

In order to correctly reference this scholarly work, feel free to copy and paste the following:

Kah-Wee Ang, Guo-Qiang Lo and Dim-Lee Kwong (2010). Germanium Photodetector Technologies for Optical Communication Applications, Semiconductor Technologies, Jan Grym (Ed.), ISBN: 978-953-307-080-3, InTech, Available from: <http://www.intechopen.com/books/semiconductor-technologies/germanium-photodetector-technologies-for-optical-communication-applications>

# **INTECH**

open science | open minds

### **InTech Europe**

University Campus STeP Ri  
Slavka Krautzeka 83/A  
51000 Rijeka, Croatia  
Phone: +385 (51) 770 447  
Fax: +385 (51) 686 166  
[www.intechopen.com](http://www.intechopen.com)

### **InTech China**

Unit 405, Office Block, Hotel Equatorial Shanghai  
No.65, Yan An Road (West), Shanghai, 200040, China  
中国上海市延安西路65号上海国际贵都大饭店办公楼405单元  
Phone: +86-21-62489820  
Fax: +86-21-62489821

© 2010 The Author(s). Licensee IntechOpen. This chapter is distributed under the terms of the [Creative Commons Attribution-NonCommercial-ShareAlike-3.0 License](#), which permits use, distribution and reproduction for non-commercial purposes, provided the original is properly cited and derivative works building on this content are distributed under the same license.